

## Modification of Fronts and Precipitation by Coastal Blocking during an Intense Landfalling Winter Storm in Southern California: Observations during CALJET

PAUL J. NEIMAN,\* P. OLA G. PERSSON,<sup>+</sup> F. MARTIN RALPH,\* DAVID P. JORGENSEN,<sup>#</sup>  
ALLEN B. WHITE,<sup>+</sup> AND DAVID E. KINGSMILL<sup>@</sup>

\*NOAA/Environmental Technology Laboratory, Boulder, Colorado

<sup>+</sup>Cooperative Institute for Research in Environmental Sciences/NOAA/ETL, Boulder, Colorado

<sup>#</sup>NOAA/National Severe Storms Laboratory, Boulder, Colorado

<sup>@</sup>Desert Research Institute, Reno, Nevada

(Manuscript received 11 February 2003, in final form 4 July 2003)

### ABSTRACT

The California Land-falling Jets Experiment (CALJET) was carried out along the California coast, and up to 1000-km offshore, during the winter of 1997/98 to study the underlying physical processes that cause flooding rains and high winds in the orographically complex coastal zone and to explore the impact of potential future observing systems on short-term (<24 h) quantitative precipitation and wind forecasts during the landfall of winter storms from the data-sparse eastern Pacific Ocean. Using the suite of experimental and operational observing systems that were available during CALJET, this study documented the mesoscale modification of an intense landfalling cyclone by the steep coastal orography on 3 February 1998. This storm heavily impacted the populous and highly vulnerable coastal zone of southern California with flooding rains, strong winds, and major beach erosion. A pair of landfalling cold-frontal zones produced most of the damaging weather, while the primary cyclone circulation remained offshore. Special attention is given to the development of blocking of the low-level flow by the steep coastal mountains of southern California and to the influence of this blocked flow on the observed nearshore frontal evolution. In particular, unique observations are presented of blocking-induced frontal splitting and frontal merging, as well as unparalleled documentation of terrain-forced frontal waves. The impact of these frontal modifications on rainfall distributions is explored. This study also provides clear observational evidence of the orographic modulation of a landfalling prefrontal low-level jet (LLJ) near the coast of southern California. This is especially important, given that LLJs efficiently transport moisture into the coastal mountains, often resulting in orographically enhanced flooding. The results described in this study have important generalized implications for understanding the complex interactions that occur between shallow blocked flows and landfalling winter storms along the mountainous west coast of North America and for understanding the impact of these interactions on rainfall, winds, and erosion in the coastal zone.

### 1. Introduction

Each winter, numerous extratropical cyclones form over the eastern Pacific Ocean, where limitations of the operational observing system make it difficult to monitor key meteorological conditions. Many of these storms strike coastal Washington and Oregon with rainfall, winds, and surf similar in intensity to conditions found in tropical storms. Hence, numerous coastal field campaigns designed to study various aspects of these storms have been carried out in this region, including the Cyclonic Extratropical Storms Project (CYCLES; Matejka et al. 1980), the Coastal Observation and Simulation with Topography Experiment (COAST I and II, Bond et al. 1997), and the Improvement of Microphys-

ical Parameterization through Observational Verification Experiment (IMPROVE I and II; Houze and Medina 2002). Farther south in California, the Sierra Cooperative Pilot Project (SCPP; Marwitz 1983; Reynolds and Kuciauskas 1988; Pandey et al. 1999) focused on wintertime orographic precipitation in the Sierra Nevada Mountains rather than along the coast, since California depends on runoff from the Sierra Nevadas for its water supply and power generation.

Because landfalling storms occur less frequently in California, few wintertime coastal field campaigns have been executed there. Nonetheless, California's storms can be as powerful as their northern counterparts, and they can be even more destructive since California is the most populous state in the nation with a majority of its citizens living and working in or near the vulnerable coastal zone (i.e., ~100 km on either side of the coastline). Hence, the California Land-falling Jets Experiment (CALJET; Ralph et al. 1999) was carried out along the California coast, and up to 1000 km off-

---

Corresponding author address: Paul J. Neiman, NOAA/Environmental Technology Laboratory, Mail Code R/ET7, 325 Broadway, Boulder, CO 80305.  
E-mail: Paul.J.Neiman@noaa.gov

shore, during the winter of 1997/98 to study the physical processes that cause flooding rains and high winds in the orographically complex coastal zone and to explore the impact of potential future observing systems on short-term (<24 h) quantitative precipitation and wind forecasts during the landfall of winter storms. Research findings from CALJET cover a range of topics, including coastal orographic precipitation and bulk microphysics (Neiman et al. 2002; White et al. 2003), sensitivity of flooding to low-level wind direction (Nuss and Miller 2001; Ralph et al. 2003), the connection between climate-scale forcing and mesoscale response (Ralph et al. 2003; Andrews et al. 2004), snow-level detection for forecasting applications (White et al. 2002), and the impact of parameterization schemes on simulated landfalling mesoscale features (Michelson and Bao 2001).

The CALJET winter of 1997/98 coincided with a high-amplitude El Niño event and was characterized by frequent and strong storms impacting the California coast. One of the strongest of these storms occurred on 2–3 February 1998, causing hurricane-force wind gusts, extensive flooding, landslides, widespread coastal erosion, and several deaths (e.g., NCDC 1998). As part of a suite of experimental and operational observing platforms available during CALJET, a National Oceanic and Atmospheric Administration (NOAA) P-3 aircraft and a network of wind profilers provided unique mesoscale observations of this storm in the coastal zone adjacent to the steep terrain. Two landfalling cold-frontal zones produced most of the damaging weather, while blocking of the low-level flow by the coastal mountains impacted the nearshore frontal evolution and rainfall distributions.

Previous studies have explored the modification of fronts and their precipitation features by mountain barriers and associated blocked flows. A unifying theme of these studies is the deceleration and/or retardation of surface fronts and associated precipitation upstream of the high terrain, first reported by Bjerknes and Solberg (1921) offshore of Norway's coastal mountains. This behavior has been reported in many other mountainous regions, including the European Alps (Kurz 1990; Egger and Hoinka 1992), the Appalachian Mountains of the eastern United States (O'Handley and Bosart 1996; Schumacher et al. 1996), and the coastal mountains of western Canada (Doyle and Bond 2001; Yu and Bond 2002), the Pacific Northwest (Braun et al. 1997, 1999a,b), and central/northern California (Doyle 1997; Yu and Smull 2000; Colle et al. 2002). The review article by Egger and Hoinka (1992) cites theoretical studies describing an inverse relationship between the magnitude of the Froude number and the degree of frontal retardation. An analogous relationship exists between the Froude number and the degree of upstream blocking; namely, blocking typically occurs when the Froude number is small (Pierrehumbert and Wyman 1985; Smolarkiewicz and Rotunno 1990). Hence, blocking pro-

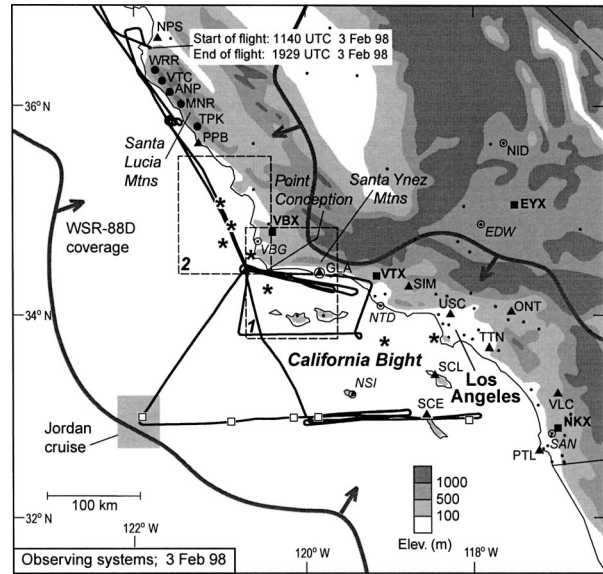


FIG. 1. Terrain base map of southern California showing the locations of key observing systems (▲ = wind profilers; ■ = operational WSR-88D radars; ○ = rawinsondes; — = P-3 flight track; □ = P-3 drosondes; \* = moored buoys; ● = METAR and RAWS surface sites; ● = ALERT rain gauges). A more detailed depiction of the terrain is provided in Fig. 28a. Only five ALERT rain gauge sites within the domain are shown and labeled; all ALERT sites with usable data are marked in Fig. 5. The bold gray-shaded lines outline the approximate useful coverage of the WSR-88D radars in the coastal zone during the storm of 3 Feb 1998. The gray-shaded box shows the domain of the research vessel *D. S. Jordan* on 3 Feb. The dashed inset boxes labeled 1 and 2 define the domains of the airborne dual-Doppler analyses in Figs. 17 and 26, respectively.

vides an environment favorable for the deceleration/retardation of approaching fronts.

To date, there have not been any comprehensive observational studies examining the impact of coastal orography on landfalling wintertime fronts in the vicinity of the California Bight and the populous Los Angeles basin. Unlike the quasi-two-dimensional coastal orography along much of the west coast of North America, the terrain is decidedly more complex in southern California. Specifically, the steep east–west Santa Ynez Mountains along the north coast of the Bight intersect a northwest–southeast range inland from Point Conception (Fig. 1). The east–west barrier is nearly orthogonal to the orientation of many of the landfalling cold fronts and impinging prefrontal southerly component flow. This is in stark contrast to observations farther north (cited earlier), where the generally north–south coastal terrain is quasi-two-dimensional and forms an acute angle with the orientation of landfalling cold fronts and the prefrontal flow. Hence, blocking and its impact on modifying the evolution of landfalling fronts may be quite different in southern California, including in the coastal zone north of the abrupt change in terrain orientation near Point Conception.

By using the CALJET observational datasets of the 2–3 February storm, the impact of the coastal terrain

on blocking and on the nearshore mesoscale frontal evolutions and rainfall distributions in this populous and complex geographic area will be explored. Emphasis will be placed on unique observations of blocking-induced frontal splitting and frontal merging, as well as unparalleled documentation of terrain-forced frontal waves. This study also provides the clearest observational evidence to date of the orographic modulation of a landfalling prefrontal low-level jet (LLJ). This is especially important, given that LLJs efficiently transport moisture into the coastal mountains, resulting in orographically enhanced flooding (Neiman et al. 2002; Ralph et al. 2003).

## 2. Observing systems

A suite of research observing platforms was deployed for CALJET across coastal California and the data-sparse eastern Pacific and California Bight (Ralph et al. 1999), complementing the established operational observing systems (see Fig. 1). Data were collected from twelve 915-MHz boundary layer wind profilers (Ecklund et al. 1988; Carter et al. 1995) within the domain of Fig. 1, including six [Piedras Blancas (PPB), Goleta (GLA), Los Angeles (USC), Tustin (TTN), Catalina Island (SCL), San Clemente Island (SCE)] deployed by NOAA's Environmental Technology Laboratory (ETL), one (NPS) operated by the Naval Postgraduate School, and four operated by California's South Coast Air Quality Management District. These profilers provided ~6-min and hourly averaged vertical profiles of horizontal wind velocity from 0.1 to 4.0 km above ground with  $\leq 100$ -m vertical resolution in clear, cloudy, and precipitating conditions. The ETL winds were objectively edited using the vertical-temporal continuity method of Weber et al. (1993). At the ETL and NPS profiler sites, a tipping-bucket rain gauge measured rainfall with 0.01-in (~0.25 mm) resolution, and observations of wind, temperature, moisture, and pressure were collected from a 10-m tower, all with 2-min sampling.

A NOAA P-3 research aircraft measured standard meteorological parameters every second during two flights. The flight on 2 February 1998 (1026–1834 UTC) released nine global positioning system dropsondes ~1000 km offshore of California, and the flight on 3 February (1140–1929 UTC) released five dropsondes over the California Bight. The dropsondes provided high-resolution vertical profiles of wind velocity, temperature, and water vapor. Remote measurements of reflectivity and radial velocity from a helically scanning tail-mounted X-band (~3.2-cm wavelength) radar provided measurements of reflectivity and Doppler motions within precipitation elements. This scanning strategy produced alternating fore- and aft-pointing range-height indicator (RHI) scans directed ~19.5° fore and aft of a baseline orthogonal to the aircraft heading (Jorgensen et al. 1996). These fore/aft RHIs were synthesized into pseudo-dual-Doppler volume renderings of the flow

field (Jorgensen et al. 1996) within the domain of the two dashed boxes in Fig. 1.

Hourly surface meteorological data were obtained from operational METAR (aviation routine weather reports) and remote automated weather station (RAWS) sites and moored and drifting buoys (including 10-min-resolution wind data from many moored buoys), 3-h meteorological data were acquired from ships (including 10-s meteorological data during a 3-week research cruise on the *D. S. Jordan* carried out by Scripps Institution of Oceanography), and operational rawinsondes provided 12-h sampling of the troposphere. Special rawinsondes were released at Pt. Mugu (NTD) and San Nichols Island (NSI) by the U.S. Navy. California's Automated Local Evaluation in Real Time (ALERT; Mendell 1992) network of ~900 rain gauges measured rainfall with 0.04-in (~1.0 mm) resolution as frequently as every 15 min. Weather Surveillance Radar-1988 Doppler (WSR-88D) scanning S-band (~10-cm wavelength) Doppler radars (Crum et al. 1993; Klazura and Imy 1993) continuously monitored the evolution of landfalling precipitation features and their radial-velocity signatures. The radial velocities were synthesized into vertical profiles of the horizontal wind with ~300-m vertical resolution using the velocity-azimuth display technique (Browning and Wexler 1968; Rabin and Zrnich 1980). Geostationary Operational Environmental Satellites (GOES) provided hourly infrared, visible, and water vapor observations and 3-hourly tropospheric feature-tracked winds (e.g., Velden et al. 1997; Nieman et al. 1997). Polar-orbiting satellites measured integrated precipitable water vapor, surface wind speed, integrated cloud liquid water, and rain rate in 400-km-wide swaths several times daily over the eastern Pacific Ocean with its Special Sensor Microwave Imager (SSM/I) instrument (Wentz 1997). Finally, commercial aircraft provided reports of temperature and wind velocity through the Aircraft Communications, Addressing, and Reporting System (ACARS; Schwartz et al. 2000).

## 3. Synoptic evolution

The synoptic evolution of the 2–3 February storm is presented to establish the large-scale context for the subsequent mesoscale discussions. Low-level (<300 m MSL) P-3 observations offshore on 2 February were combined with ship, buoy, wind profiler, and METAR data to generate surface analyses of potential temperature ( $\theta$ ), equivalent potential temperature ( $\theta_e$ ), and sea level pressure (SLP) over the open ocean (Fig. 2). The analyses show two cold fronts, each associated with enhanced dry and moist baroclinicity. The leading or “primary” cold front marked the western terminus of a warm and moist warm sector ( $\theta > 292$  K;  $\theta_e > 320$  K) of subtropical origin; the northern terminus of the warm sector was bounded by a prominent warm front. Farther west, a trailing or “secondary” cold front was situated at the forward edge of a deep-tropospheric cold-

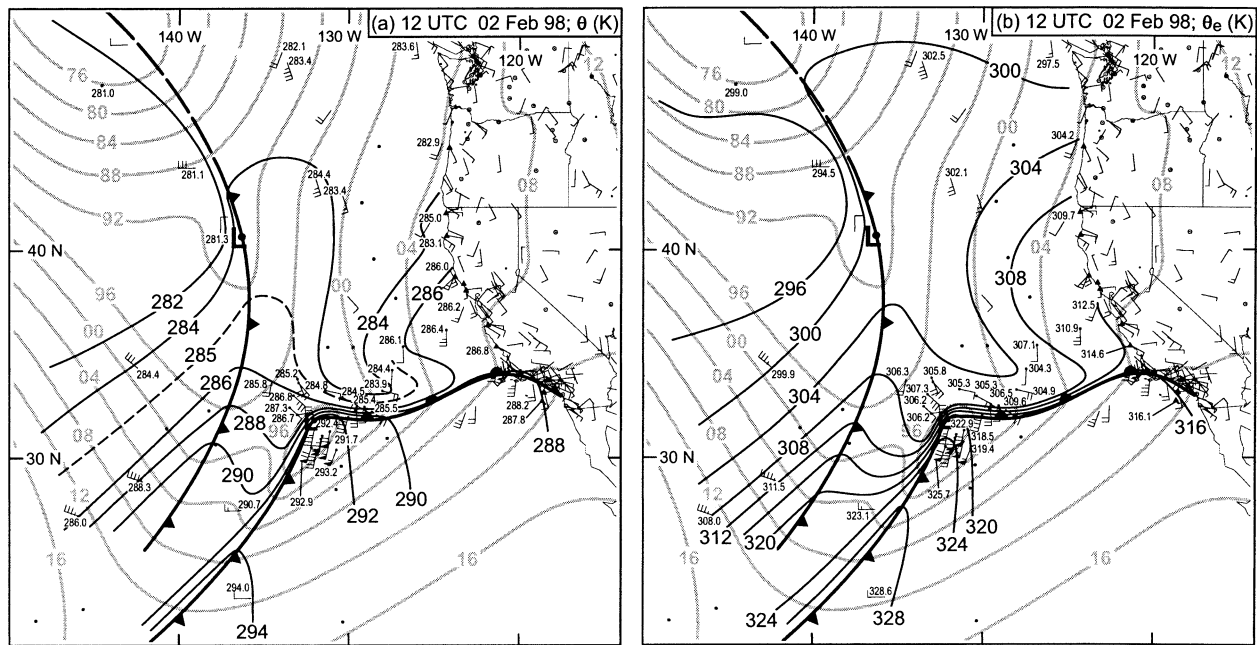


FIG. 2. Surface analysis of (a) potential temperature  $\theta$  (K, black), and (b) equivalent potential temperature  $\theta_e$  (K, black), at 1200 UTC 2 Feb 1998. The sea level pressure analysis (SLP, gray shaded) is also shown. Wind flags are  $25 \text{ m s}^{-1}$ , full barbs are  $5 \text{ m s}^{-1}$ , and half-barbs are  $2.5 \text{ m s}^{-1}$ . The land-based observations are from METAR sites (no vector heads) and profiler sites (triangle vector heads). The ocean-based observations are from ships and buoys [no vector heads or stand-alone solid dots (SLP-only reports)], and from time-to-space adjusted P-3 near-surface dropsonde data and low-level (<300 m MSL) flight legs (dot vector heads). All offshore values of  $\theta$  and  $\theta_e$  are plotted, except for selected  $\sim 300 \text{ m MSL}$  P-3 observations. Standard frontal notation is used.

core air mass. Although the P-3 did not penetrate the secondary front, it observed the front's precipitation band (>250 km in meridional extent and 50 km in width) about 250 to 300 km west of the primary front.

A series of SLP analyses on 3 February (Fig. 3) were derived from ship, buoy, wind profiler, and METAR observations, and from P-3 observations in the coastal zone. GOES feature-tracked winds (Fig. 4) and SSM/I products (not shown) provided additional constraints to finalize the SLP analyses. Figures 3 and 4 show the two cold fronts impacting California between 0600 and 1800 UTC 3 February. Cyclogenesis occurred along the secondary front over the ocean between 0000 and 0600 UTC 3 February. An evolving comma-cloud head coincided with the surface cyclone position, which remained offshore. This study will focus on the orographic modification of these two landfalling cold fronts and their precipitation distributions within the inset domain of Fig. 3.

An accumulated rainfall analysis between 0000 and 2100 UTC 3 February (i.e., during the period of frontal landfall) is presented in this inner domain (Fig. 5). Substantial rain (>25 to 50 mm) fell across the coastal zone. The heaviest rains were focused in the coastal mountains, thus revealing the significance of orographic forcing during this event (Neiman et al. 2002; Ralph et al 2003). Most of the rainfall was associated with one or more of the rainbands portrayed in Fig. 6, except for a

pseudo-warm-frontal "intermediate rainband" that remained offshore.

The NOAA P-3 transected these bands (see Fig. 6), providing crucial data to document the vertical structure of the primary and secondary cold fronts along the line AA' away from orographic influences. Cross sections of  $\theta$ , meridional (i.e., alongfront) wind, and  $\theta_e$  (Fig. 7) were augmented by 6-min data from the island wind profiler at SCE (Fig. 8), which also resided beyond the influence of the coastal orography. The cross sections and profiler data show the primary cold front extending upward from the sea surface (west of Drop 1420 in Fig. 7a) and sloping westward with height. The front was vertical below  $\sim 750 \text{ mb}$  in the vicinity of a convective squall line (band 2a;  $\sim 32 \text{ mm h}^{-1}$ ). A trailing zone of stratiform rain<sup>1</sup> was situated to its west (band 2b) in a configuration typical of a continental mesoscale convective system (MCS; Biggerstaff and Houze 1993). The back edge of the stratiform rain coincided with a minimum in surface pressure at SCE (Fig. 8b), characteristic of a "wake low" in MCSs (Stumpf et al. 1991; Loehrer and Johnson 1995). Another common feature of MCSs was also observed at SCE, namely a rear inflow

<sup>1</sup> The precipitation characteristics at SCE were ascertained through detailed inspection of the 6-min spectral moment data (not shown), which differentiated between convective and stratiform regimes (e.g., Ralph et al. 1995).

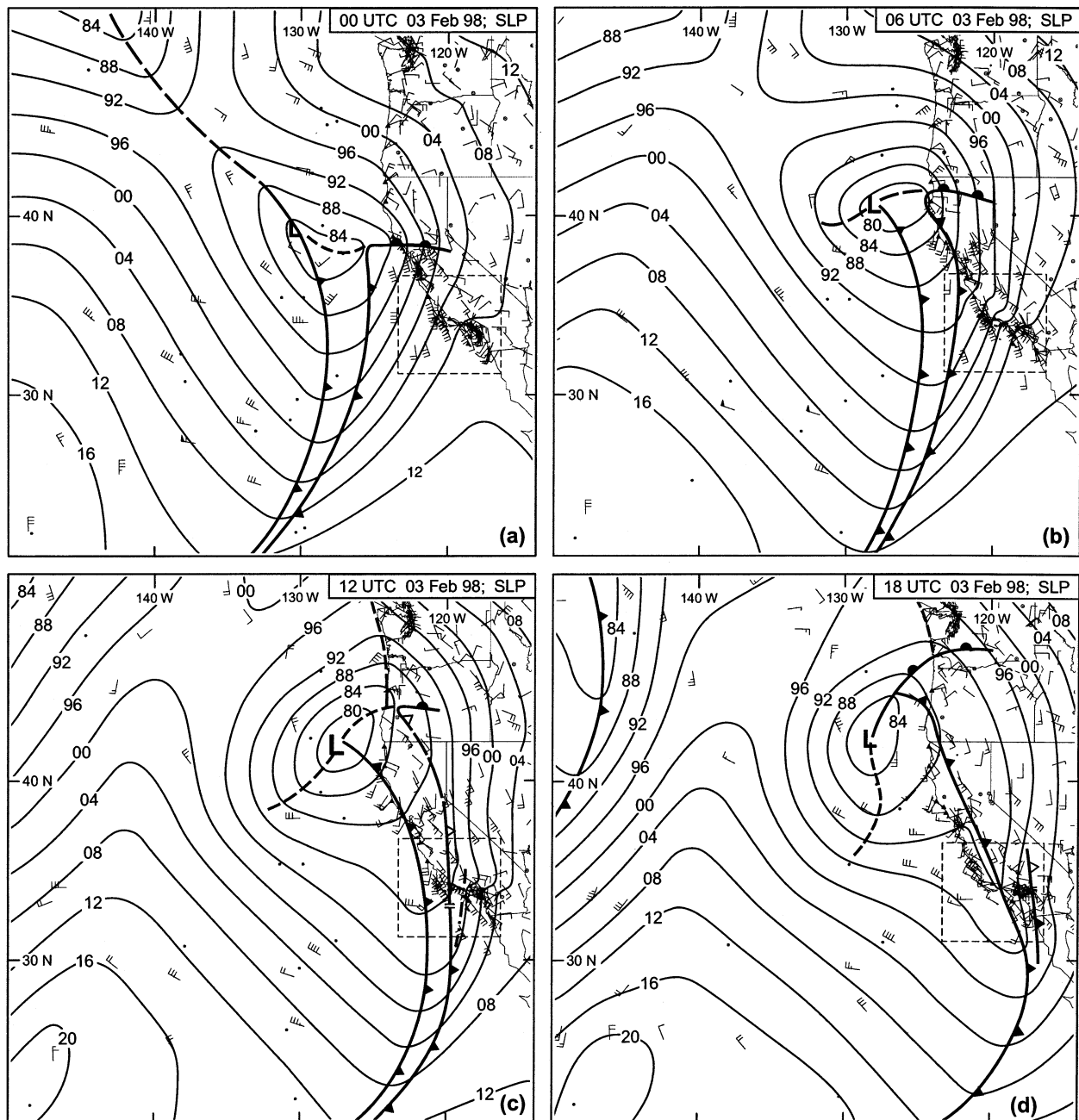


FIG. 3. SLP analysis at (a) 0000, (b) 0600, (c) 1200, and (d) 1800 UTC 3 Feb 1998. Wind barbs, observing system conventions, and frontal notations are as in Fig. 2. Open frontal symbols portray fronts above the surface. The dashed inset domain is used in Figs. 1, 5, 12, and 13.

jet (e.g., Smull and Houze 1987) near the rear of the stratiform rain (centered at 1525 UTC and 2.3 km MSL). The MCS with the primary front quite likely altered the front's classical structural characteristics (e.g., Browning and Harrold 1970).

To the east of the primary front, a long-lived prefrontal squall line (band 1) was observed (Figs. 7, 8). A 1-K decrease in surface  $\theta$  with the prefrontal squall was half as large as with the primary front. In addition,

the speed and directional shear across the prefrontal squall at SCE was much smaller than across the primary front. The cross-front or zonal component of the airflow at SCE (time-to-space adjusted using the same phase velocity as in Fig. 6) was used to compute the two-dimensional divergence (not shown). This computation showed that convergence with the prefrontal squall was only present aloft between 1.5 and 3.0 km MSL, similar to what Parsons and Hobbs (1983) found for steady-

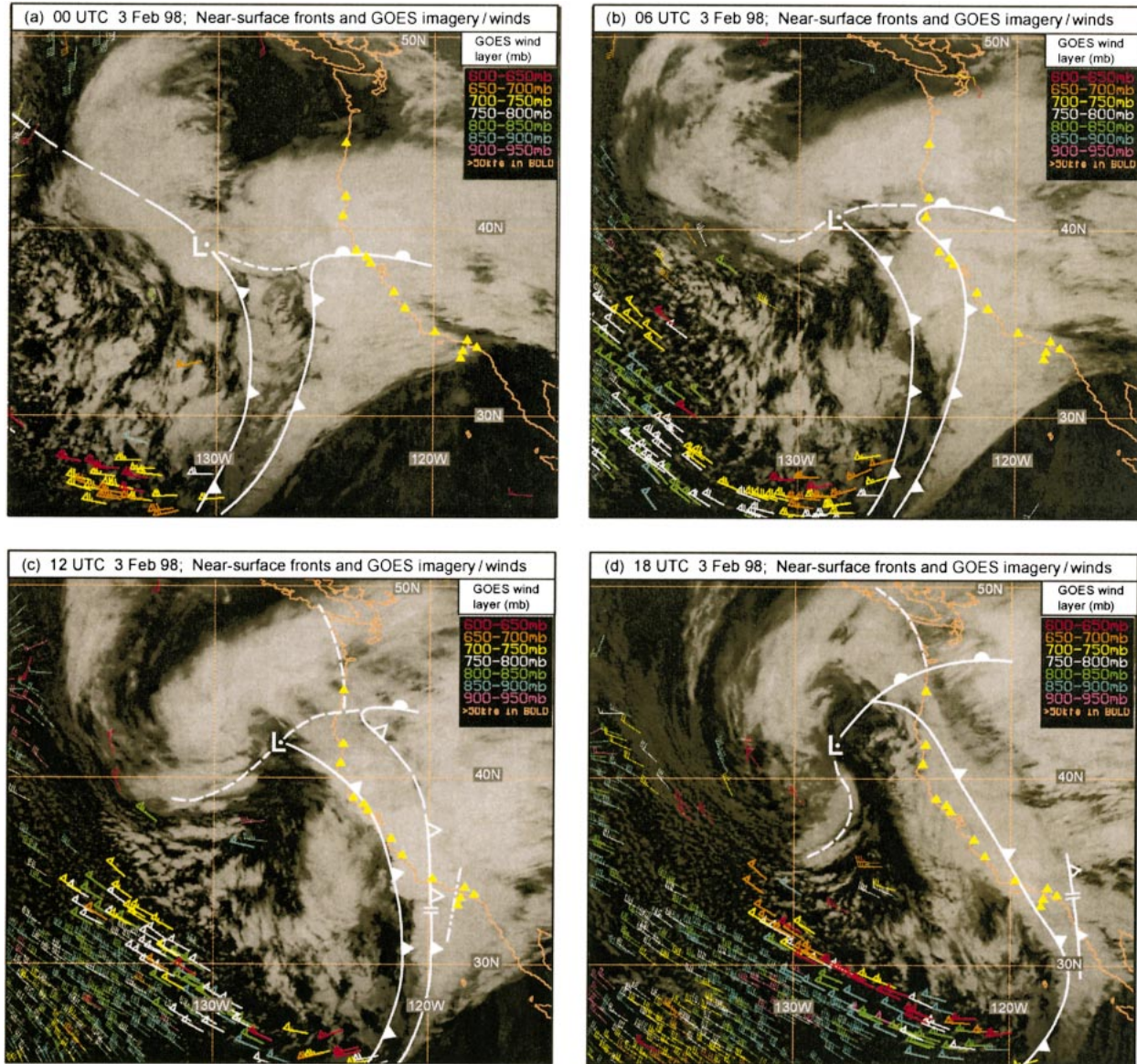


FIG. 4. NOAA GOES infrared satellite images with frontal positions at (a) 0000, (b) 0600, (c) 1200, and (d) 1800 UTC 3 Feb 1998. Satellite-derived feature-tracked winds below 600 mb are shown (wind flags and barbs are as in Fig. 2). The NOAA/ETL coastal wind profiler array, supplemented by the NPS profiler near Monterey, is shown with the string of yellow triangles.

state, warm-sector rainbands. In contrast, the primary frontal squall line was accompanied by organized convergence below  $\sim 1$  km MSL, similar to observations along narrow cold-frontal rainbands (NCFRs) by Hobbs and Biswas (1979), among others. A moist ( $\theta_e > 318$  K) southerly LLJ of  $\sim 34$  m s $^{-1}$  at 900 mb (1 km MSL) ahead of the prefrontal squall line was embedded in a favorable thermal gradient opposite to that of the cold fronts and mirrored the prefrontal LLJ attributes observed 1000 km offshore the previous day (Persson et al. 1999; Ralph et al. 2003). Hence, the prefrontal LLJ environment did not change appreciably over the ocean during this period. An upper-level jet streak penetrated

downward to  $\sim 700$  mb on the warm side of the primary front, though its spatial continuity was interrupted in the vicinity of the primary frontal squall line (band 2a). Immediately to the west of the primary front, weaker southwesterly flow ( $< 20$  m s $^{-1}$ ) below  $\sim 850$  mb was observed in a region where  $\theta_e$  decreased to  $\sim 313$  K. The cool sector was potentially unstable ( $-\partial\theta_e/\partial p < 0$ ), except within the shallow westward-sloping secondary cold front and an eastward-sloping pseudo-warm front. Moderate winds ( $\sim 15$  m s $^{-1}$ ) shifted from southerly to westerly across the secondary front, where a shallow rainband was observed at its leading edge (band 4). An LLJ of  $\sim 18$  m s $^{-1}$  preceded the secondary front

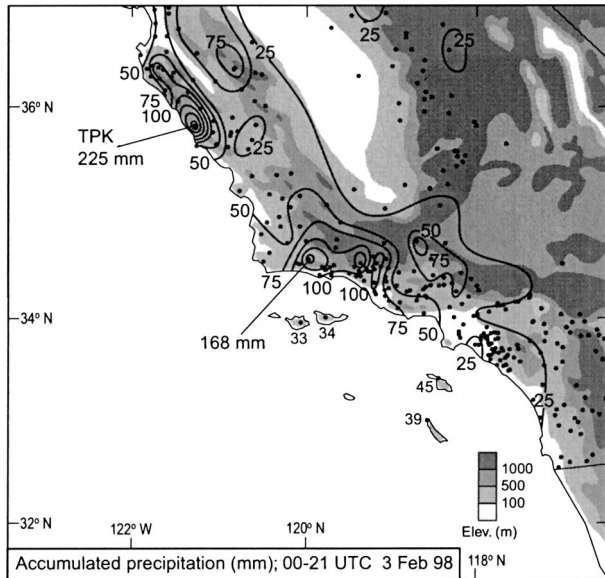


FIG. 5. Terrain base map with a 21-h accumulated rainfall analysis (mm) between 0000 and 2100 UTC 3 Feb 1998. The dots show the ALERT, METAR, RAWS, and wind profiler rain gauge sites used for the analysis. The rain gauge site at TPK is labeled.

atop the pseudo-warm front. A weak rainband (band 3) accompanied this warm front, where a 1.5-K increase in surface  $\theta$  was observed at SCE. This front generated little significant weather at the coast and will not be discussed further.

The balance of the paper will focus on documenting the complex mesoscale modification of the two land-falling cold fronts and their precipitation features and LLJs by the coastal orography of southern California. This modification is introduced here by presenting a 5-h-long sequence of WSR-88D hourly radar reflectivity images of multiple rainbands on 3 February (Fig. 9). Due to the terrain-induced mesoscale complexities, these rainbands could not be identified solely by inspection of this imagery. Rather, a detailed mesoscale analysis of this event using the CALJET datasets was required in tandem with careful examination of the radar images available every 6 min. The hourly imagery shows the prefrontal squall line moving eastward and decelerating across the eastern Bight and Los Angeles between 1027 and 1429 UTC. To its west, the primary frontal squall line developed south of GLA by 1137 UTC, subsequently intensifying while moving eastward. Prior to 1027 UTC, the low-level portion of the primary front decelerated upon reaching blocked flow trapped against the coastal mountains (not shown), and it decoupled from the transient upper portion of the front. A rainband coincided with the terrain-retarded low-level front (hereinafter referred to as the “remnant low-level primary front”) and trailed the primary frontal squall line that tracked with the transient portion of the primary front. The remnant low-level primary front was the focus for two frontal waves between 1027 and 1230 UTC

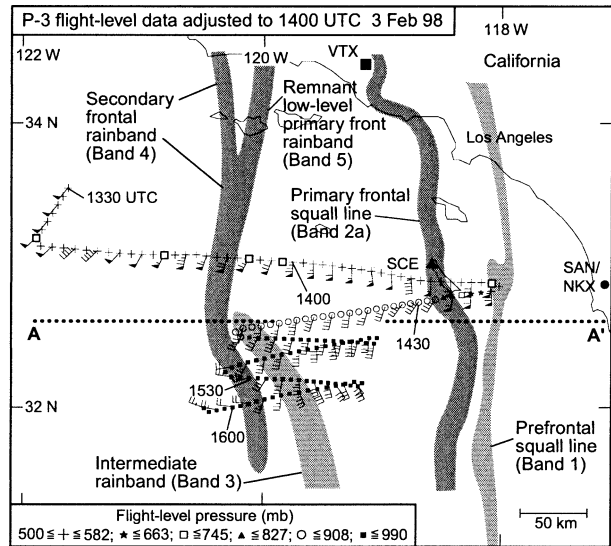


FIG. 6. Base map of the California Bight showing a NOAA P-3 flight segment and selected wind observations (flags and barbs are as in Fig. 2) on 3 Feb 1998 (times labeled every 0.5 h). The flight track (pressure coded) is time-to-space adjusted to 1400 UTC 3 Feb using a phase velocity of  $16.8 \text{ m s}^{-1}$  from  $200^\circ$ . A schematic depiction of the significant rainbands observed by the P-3 lower-fuselage radar and the VTX and NKX WSR 88D radars is shaded gray. (band numbers are as in Figs. 7–9 and 15). Dotted-line AA' is a cross-section projection for Fig. 7.

(see section 5c). Weak multibanded precipitation with the steadily advancing secondary front was merging with the slowly moving remnant primary frontal rainband at  $\sim 1429$  UTC just south of GLA. By 1531 UTC, a squall line exploded along these merging fronts as they approached GLA, where a flood-producing burst of heavy rain ( $77 \text{ mm h}^{-1}$ ) ensued.

#### 4. Blocking in the California Bight

Southern California's steep coastal orography can profoundly modify southerly flow regimes in advance of landfalling fronts during the cool season, resulting in shallow blocked flow trapped against the high terrain. Blocking deflects the low-level flow upstream and below the top of mountain ranges (Bell and Bosart 1988; Colle and Mass 1995) and results in the formation of a barrier jet below mountaintop that parallels the long axis of quasi-two-dimensional high terrain (Parish 1982; Overland and Bond 1995; Doyle 1997). Blocking can also locally redistribute precipitation, inhibit the forward motion of approaching fronts, and produce strong winds due to the superposition of a barrier jet and prefrontal LLJ (Dunn 1987; Peterson et al. 1991; Doyle 1997; Sinclair et al. 1997; Braun et al. 1999a; Doyle and Bond 2001; Yu and Smull 2002; Yu and Bond 2002; Neiman et al. 2002).

Blocking typically occurs when the Froude number ( $Fr = U/Nh$ ; where  $U$  is the barrier-normal wind speed,  $N$  is the Brunt-Väisälä frequency, and  $h$  is the barrier

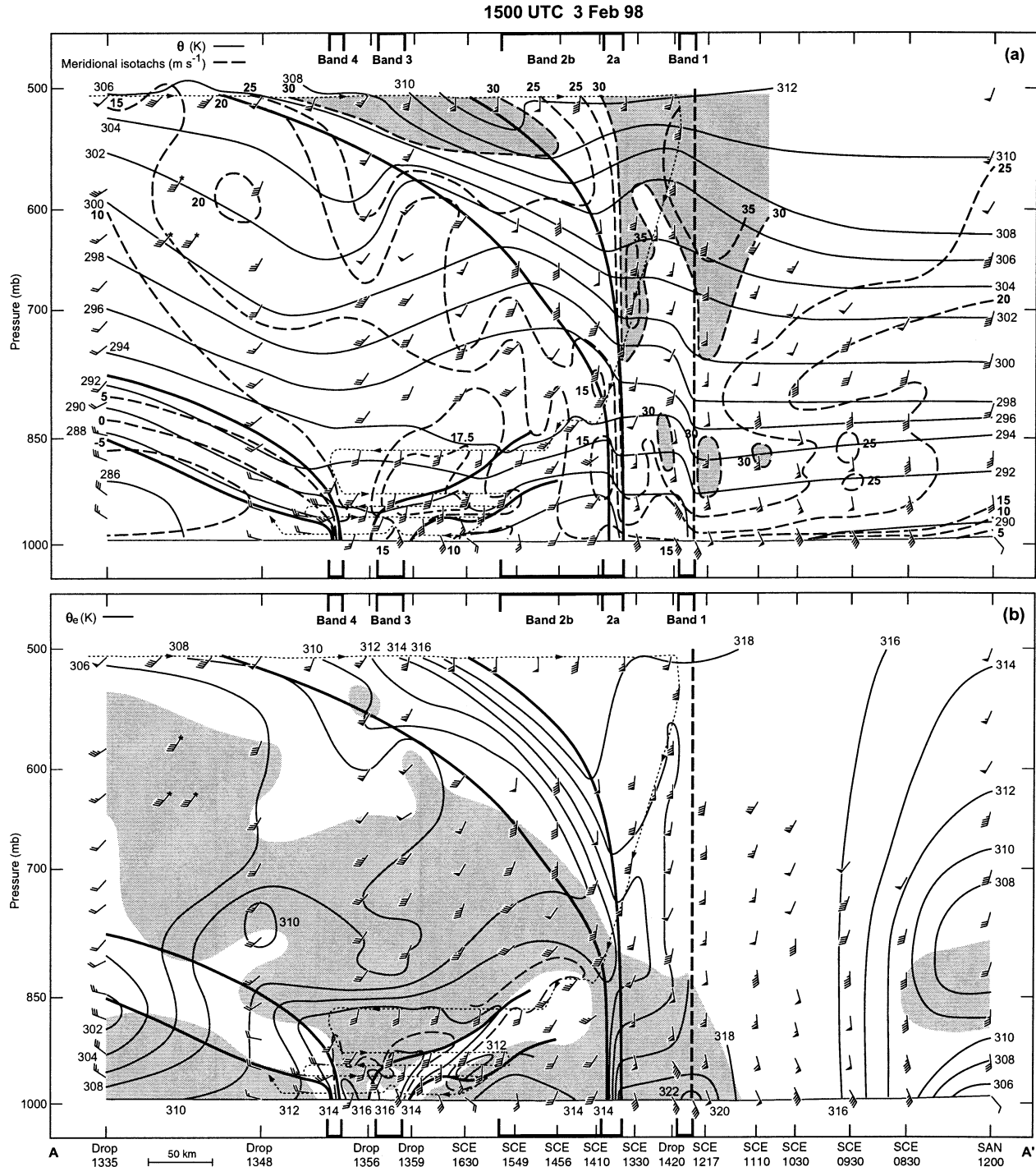


FIG. 7. Cross section of (a)  $\theta$  (K, solid) and meridional isotachs ( $m s^{-1}$ , dashed; shading  $>30 m s^{-1}$ ), and (b)  $\theta_e$  (K) and potential instability (shaded), along line AA' in Fig. 6 at 1500 UTC 3 Feb 1998. Wind flags and barbs are as in Fig. 2. Vertical tick marks correspond to time-to-space adjusted (as in Fig. 6) P-3 dropsondes ("Drop"), rawinsonde (SAN), and wind profiler data (SCE); their deployment times (UTC) are shown. The time-to-space adjusted P-3 flight track between 1335 and 1605 UTC 3 Feb 1998 is depicted with a thin dotted line, with selected flight-level wind vectors plotted. Bold solid lines are frontal boundaries, and the bold dashed-line is the prefrontal squall line. The rainbands (heavy brackets top and bottom) are the same as in Figs. 6, 8, 9, and 15.

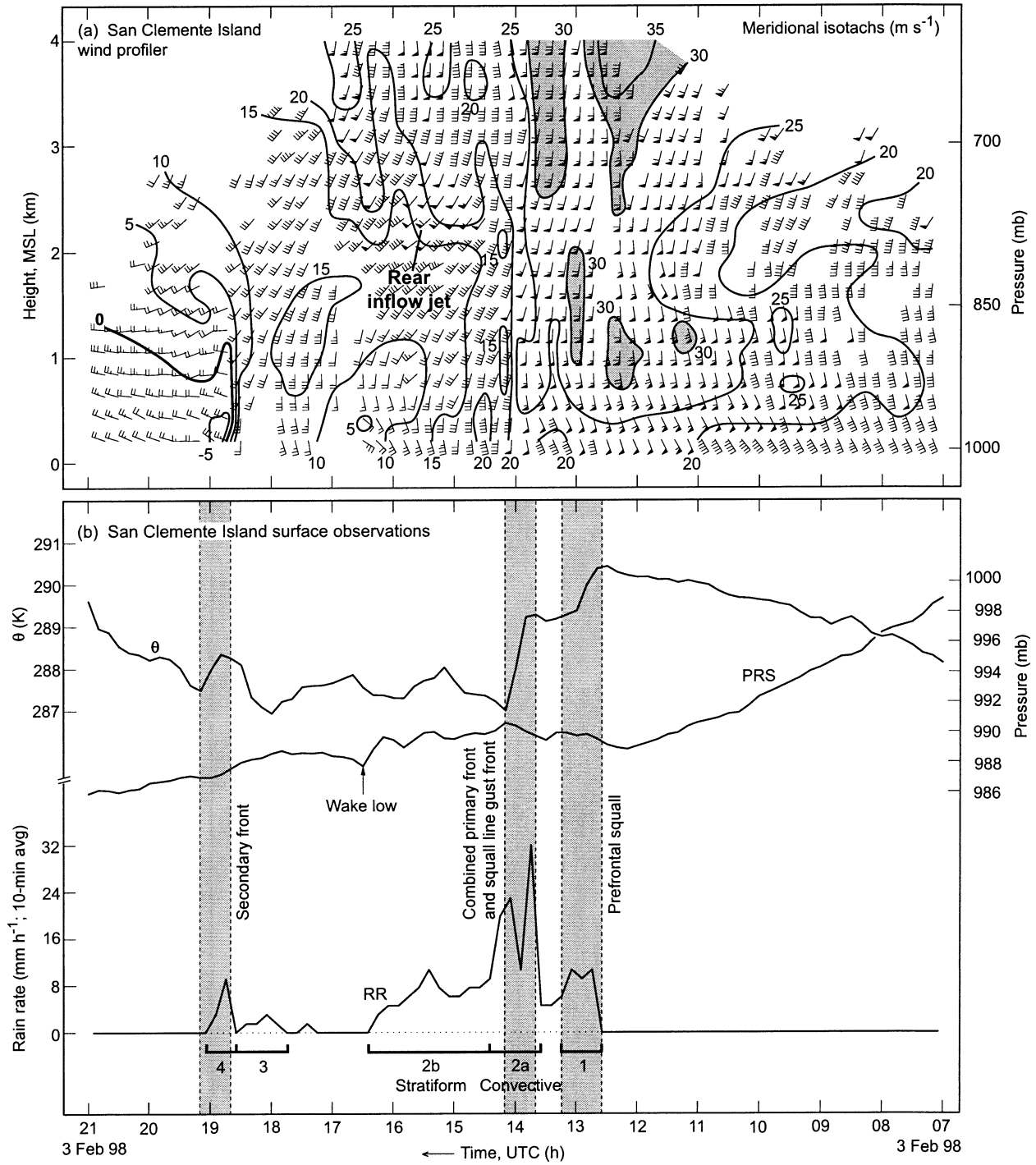


FIG. 8. Wind profiler and surface data from SCE: (a) time–height section of 6-min wind profiles (flags and barbs are as in Fig. 2; every other profile and range gate are shown) and meridional isotachs ( $\text{m s}^{-1}$ ; solid), and (b) time series of surface data [ $\theta$  = potential temperature (K); PRS = pressure (mb); RR = rain rate ( $\text{mm h}^{-1}$ ; 10-min averaging period)]. Surface wind velocity data were unavailable. The vertical gray-shaded bars bounded by dashed lines denote significant transitions. The rainbands in (b) (bold brackets) are the same as in Figs. 6, 7, 9, and 15.

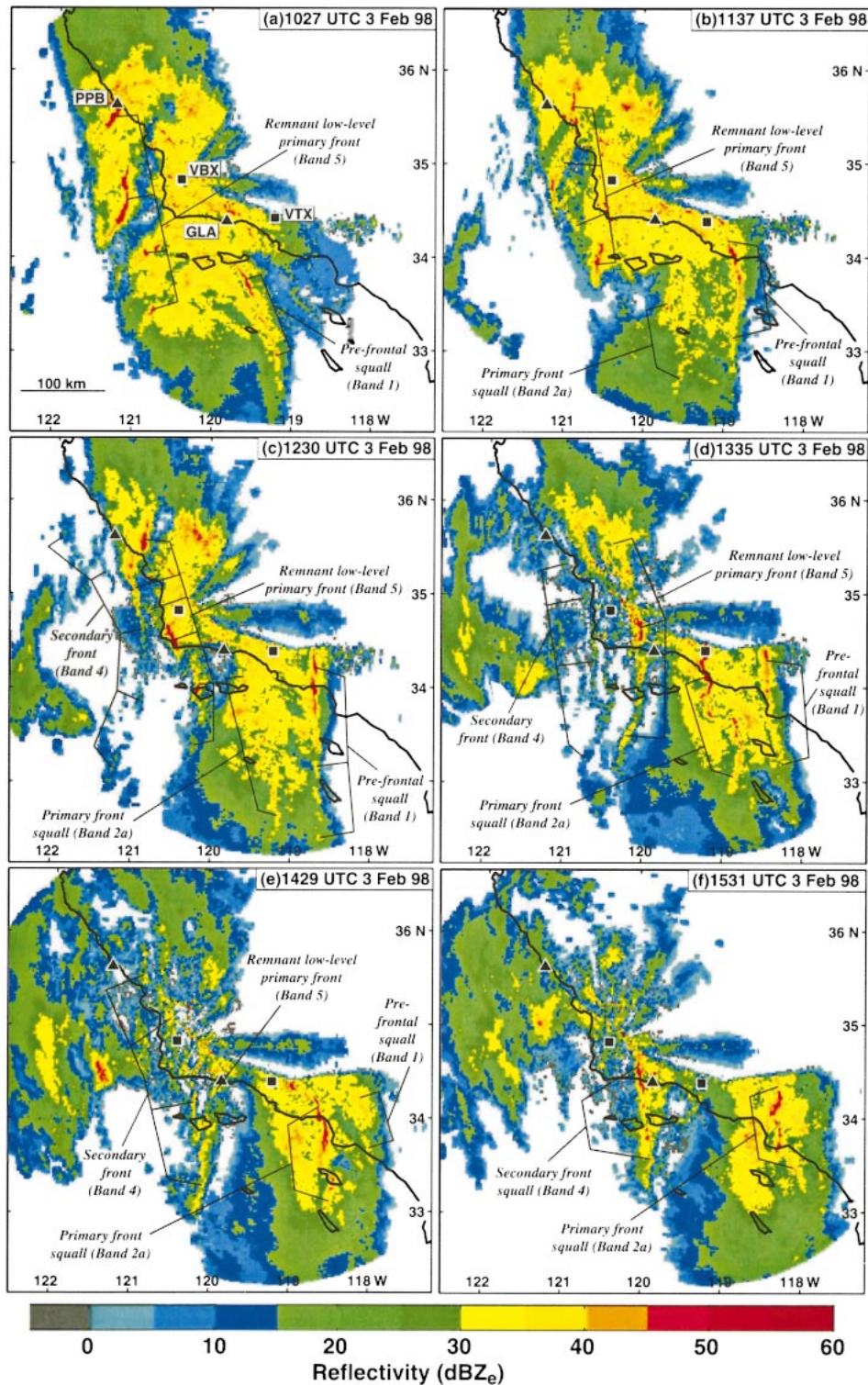


FIG. 9. Composite WSR-88D radar reflectivity (dBZ) images based on 0.5°-elevation scans from VBX and VTX at (a) 1027, (b) 1137, (c) 1230, (d) 1335, (e) 1429, and (f) 1531 UTC 3 Feb 1998. Relevant precipitation features are labeled (see also Figs. 6–8 and 15 for numbered rainbands), as are the radar sites at VBX and VTX and the wind profiler sites at GLA and PPB. Because the base elevations at VBX and VTX are 376 and 831 m MSL, respectively, their radar beams may have yielded slightly different depictions of the precipitation fields. The rainband numbers are the same as in Figs. 6, 7, 8, and 15.

height) of the flow approaching a mountain barrier is small (Pierrehumbert and Wyman 1985; Smolarkiewicz and Rotunno 1990), typically less than unity (Smith 1979). A representative Froude number for the 3 February storm was determined from the prefrontal conditions observed by a rawinsonde at 0000 UTC 3 February at San Nicolas Island (NSI in Fig. 1; not shown), about 120 km upstream of the mountainous north shore of the California Bight. Based on a 1356-m layer average between 1000 and 850 mb where south-southeasterly flow was observed,  $N = 0.0143 \text{ s}^{-1}$  and  $U = 16.7 \text{ m s}^{-1}$ . A barrier height of 1070 m was used, based on the mean of the 11 highest peaks of the coastal Santa Ynez mountains. Hence,  $Fr = 1.09$ . This value is near the minimum threshold of 1, thus indicating that conditions were conducive to flow blocking. If the higher terrain ( $>1500 \text{ m}$ ) slightly inland is considered,  $Fr$  would decrease to 0.78.

Wind profiler data from two coastal sites (Figs. 10a,b) and an island site about 80 km away from the high terrain (Fig. 10c) reveal an easterly deflection of the low-level preprimary-frontal flow at the coast relative to the ambient southerly flow offshore, thus highlighting the presence of blocked flow and its limited offshore extent. Comparison of 6-h averaged wind profiles in the LLJ region ahead of the primary front (Fig. 11) further differentiate between the blocked and unperturbed flows. The mean wind direction profiles (Fig. 11a) show the blocked coastal flow at the surface nearly parallel to the barrier orientation. From the surface to mountaintop, the wind direction profiles show the easterly deflection of the flow at the coast, decreasing with height. Above mountaintop, the coastal and offshore wind directions were more similar, although a  $10^{\circ}$ – $15^{\circ}$  wind direction offset was observed above mountaintop between the coastal sites and the more southern island site due to the presence of large-scale cyclonically curved flow. The directional vertical wind shear at the coast (Fig. 11b) was maximized in a clockwise sense near mountaintop and marked the top of the blocked flow.

Profiles of the zonal wind difference between the coastal and island sites (Fig. 11c) reveal classical barrier-jet perturbation structure, with a peak magnitude of  $6$ – $8 \text{ m s}^{-1}$  at  $\sim 500 \text{ m}$  MSL directed from the east. The easterly perturbation was confined to the blocked layer beneath the mountaintop and resulted from the westward deflection of the ambient south-southeasterly flow impinging upon the east–west-oriented coastal mountain barrier. Above mountaintop, the vertical gradient of the zonal wind difference was minimal. The close proximity of SCL and USC makes for an especially useful comparison and reveals only slightly stronger easterly flow above the mountains at USC (up to 4 km, not shown) that reflects the cyclonic curvature of the flow. The GLA–SCL curve contains a  $\sim 6 \text{ m s}^{-1}$  easterly component offset arising from stronger flow as the storm first entered the Bight. The comparison between the

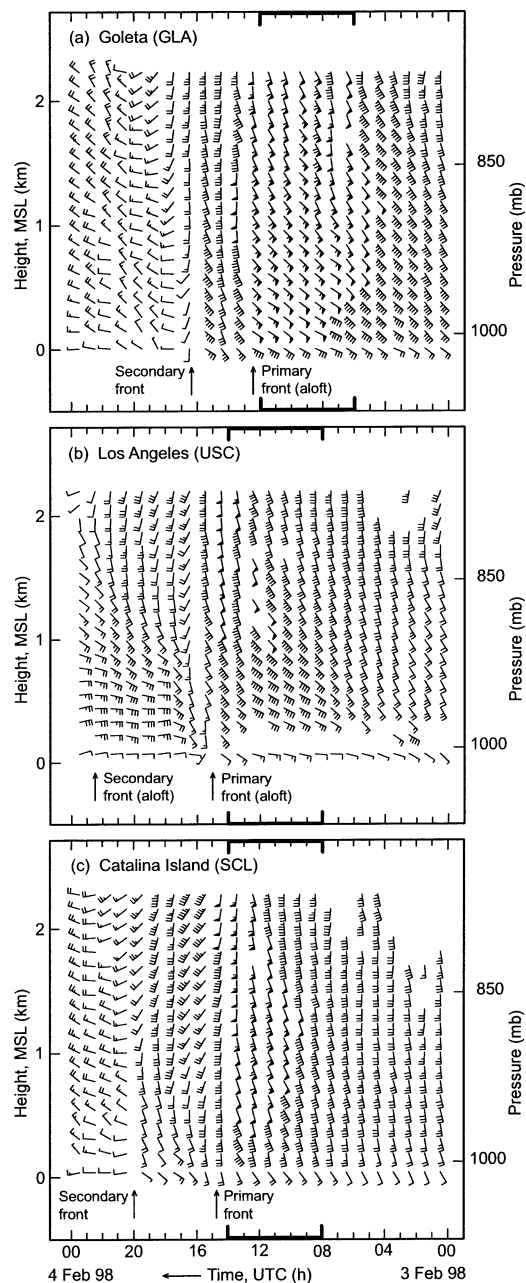


FIG. 10. Time–height sections of hourly averaged wind profiler data at (a) GLA, (b) USC, and (c) SCL. Wind flags and barbs are as in Fig. 2. Bold brackets mark the 6-h averaging periods used to create the profiles in Fig. 11. Relevant transitions are labeled.

coastal and island profilers highlight both the vertical structure and the limited offshore extent ( $<80 \text{ km}$ ) of the blocked flow on 3 February.

## 5. Impact of blocking on mesoscale frontal evolution

In this section, three types of blocking-induced frontal modification on 3 February are described: frontal split-

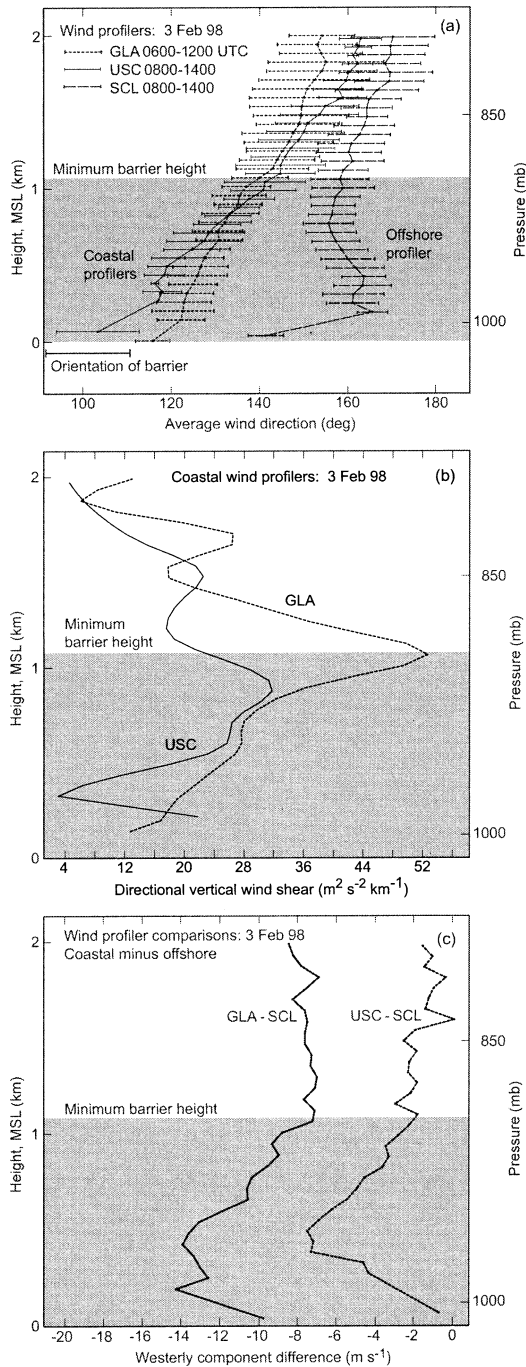


FIG. 11. (a) Vertical profiles of 6-h-averaged wind direction (deg) measured by the coastal wind profilers at GLA and USC and by the offshore profiler at SCL. (b) Vertical profiles of 6-h averaged directional vertical wind shear ( $m^2 s^{-2} km^{-1}$ ) at the coastal wind profilers. (c) Vertical profiles of 6-h-averaged zonal wind difference ( $m s^{-1}$ ) between the coastal profilers and the offshore profiler. The 6-h averaging period is defined in the key in (a) and is shown in Fig. 10. The top of the gray-shaded region defines the minimum mountain barrier height near the coastal profilers. The orientation of the local mountain barrier is marked in (a).

ting, frontal merging, and frontal waves. The impact of these on rainfall distributions and LLJ evolutions are also explored. First, however, a mesoscale synopsis of this event in southern California is presented using 3-h SLP analyses between 0300 and 2100 UTC 3 February 1998 (Fig. 12) and surface  $\theta$  analyses at 0900 and 1200 UTC (Fig. 13). The frontal analyses are supported by mesoanalyses presented later. In the absence of in situ data, the analyzed perturbations of each cold front conformed to prominent undulations along its NCFR, based on the assumption that the NCFRs marked the leading edge of the fronts (Hobbs and Biswas 1979; Hobbs and Persson 1982; Yu and Smull 2000; Chien et al. 2001) where low-level convergence is maximized.

At 0300 UTC (Fig. 12a), southwest-northeast-oriented isobars resided over the ocean, while both cold fronts and their pressure troughs were west of the analysis domain. Windward ridging associated with the blocked flow encompassed the coastal zone of the California Bight at this time, and it was maintained through the remainder of the analysis period (Figs. 12b-12g). This region exhibited downgradient flow parallel to the coastal mountains, both key characteristics of blocking. A pressure trough resided on the downstream (i.e., north) side of the coastal mountains in response to lee-side mountain wave activity (e.g., Smith 1979; Durran 1986). Companion 3-h precipitation analyses show the greatest rainfall over land occurred near the fronts and in the coastal mountains.

The primary and secondary cold fronts approached California between 0600 and 0900 UTC. By 1200 UTC, the low-level portion of the primary front had decelerated upon reaching the shallow blocked flow, while the upper-level portion of this front migrated eastward aloft such that the front split in the vertical [see section 5a(1)]. Between 1200 and 1500 UTC, the remnant low-level primary front was positioned between its parent front to the east and the impinging secondary front to its west. Three commercial aircraft flew through the primary front aloft between 1500 and 1800 UTC (tracks shown in Figs. 12e,f; the bold segment of each track is where the aircraft descended through the primary front aloft) and provided data above the complex terrain (Fig. 14). The soundings show classical frontal structure with the primary front above  $\sim 700$  mb, including enhanced stratification and strong directional vertical wind shear indicative of cold advection, thus revealing that the terrain did not impact the frontal structure aloft. Two of these soundings also show enhanced stratification and vertical wind shear within the shallow blocked flow.

The blocked flow is highlighted further in companion surface  $\theta$  analyses at 0900 and 1200 UTC (Fig. 13). These analyses, which were augmented by the detailed examination of buoy time series traces and P-3 data, show cool air from the interior extruding westward in a narrow blocked plume across the Los Angeles Basin and along the north coast of the Bight. The blocked flow reached an equilibrium temperature with the underlying

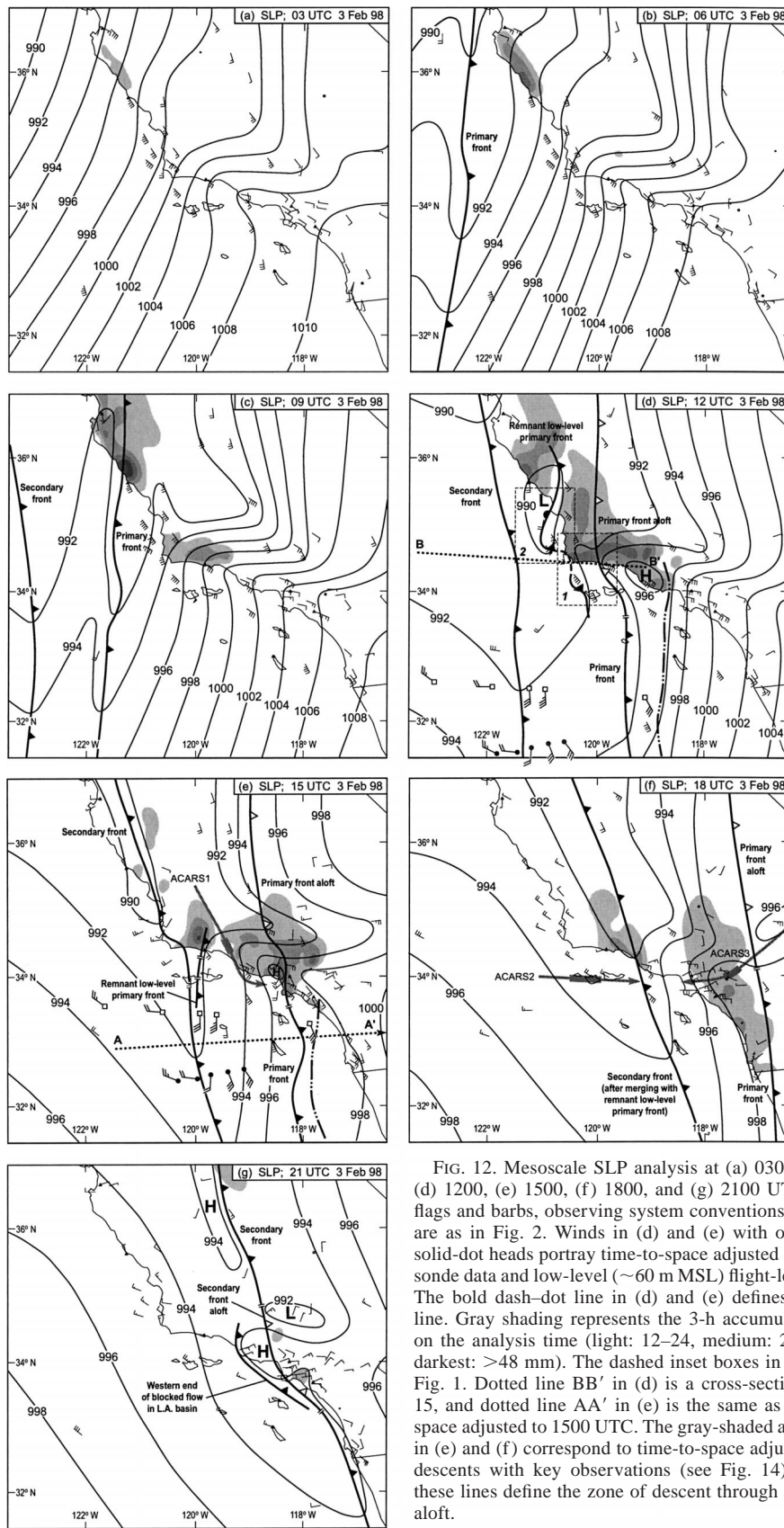


FIG. 12. Mesoscale SLP analysis at (a) 0300, (b) 0600, (c) 0900, (d) 1200, (e) 1500, (f) 1800, and (g) 2100 UTC 3 Feb 1998. Wind flags and barbs, observing system conventions, and frontal notations are as in Fig. 2. Winds in (d) and (e) with open-square heads and solid-dot heads portray time-to-space adjusted P-3 near-surface dropsonde data and low-level (~60 m MSL) flight-level data, respectively. The bold dash-dot line in (d) and (e) defines the prefrontal squall line. Gray shading represents the 3-h accumulated rainfall centered on the analysis time (light: 12–24, medium: 24–36, darker: 36–48, darkest: >48 mm). The dashed inset boxes in (d) are the same as in Fig. 1. Dotted line BB' in (d) is a cross-section projection for Fig. 15, and dotted line AA' in (e) is the same as in Fig. 6 but time-to-space adjusted to 1500 UTC. The gray-shaded arrows labeled ACARS in (e) and (f) correspond to time-to-space adjusted commercial flight descents with key observations (see Fig. 14); the bold portion of these lines define the zone of descent through the primary cold front aloft.

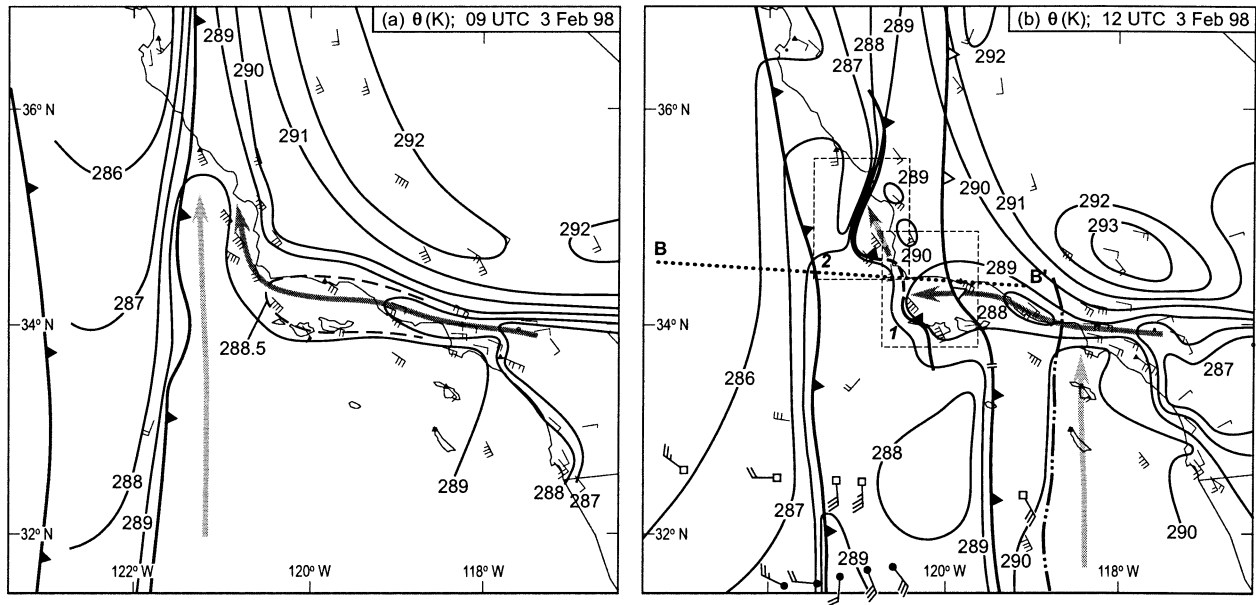


FIG. 13. Mesoscale surface  $\theta$  analysis (K) at (a) 0900 and (b) 1200 UTC 3 Feb 1998. Wind flags and barbs, observing system conventions, frontal notations, line BB', and the dashed boxes are as in Fig. 12. Dark and light gray-shaded lines portray the blocked and prefrontal airstreams, respectively.

sea surface ( $\sim 289$  K) after turning northward around Point Conception in the vicinity of the warm airstream ahead of the primary front at 0900 UTC. By 1200 UTC, an isolated pocket of warm air ( $> 289$  K) was trapped between the remnant low-level primary front and the high terrain north of Point Conception. It possessed thermodynamic and kinematic attributes consistent with the mixing of the ocean-modified blocked flow and prefrontal airstream. A tight  $\theta$  gradient was observed northwest of the remnant low-level primary front, while a modest  $\theta$  gradient accompanied each of the other boundaries. Figure 13b depicts the fronts highlighted in this paper, but because diabatic processes in the boundary layer (e.g., sea surface fluxes, evaporation, the diurnal cycle) tend to weaken the surface  $\theta$  gradients across these fronts, the ensuing mesoscale discussion will focus on conditions aloft where the gradients are stronger.

The secondary cold front marked the transition between southerly-component flow to its east and northwesterly flow to its west (Figs. 12d–12g). Between 1500 and 1800 UTC, the secondary front overtook the remnant low-level primary front in the north Bight region. Thereafter, it scoured out the blocked easterly flow during its eastward migration, except after 1800 UTC when the secondary front split in the vertical over the blocked flow in the Los Angeles Basin.

*a. Frontal splitting*

1) PRIMARY COLD FRONT

A cross section over the California Bight was presented in section 3 (Fig. 7), highlighting the downward

penetration of the primary cold front to the surface and the presence of a prefrontal LLJ, similar to what was observed 1000 km offshore the previous day. That analysis represents a crucial baseline comparison with a second section through the same front along the mountainous north coast of the California Bight (Fig. 15). Similarities between these sections include: 1) a westward-sloping primary cold-frontal zone between 800 and 500 mb, 2) a postprimary-frontal intrusion of low- $\theta_e$  air above 800 mb, 3) a near-surface layer of high- $\theta_e$  air ahead of the primary front, 4) a shallow layer of potential instability ahead of the primary front that deepened on its cold side, and 5) a downward extension of the upper-level jet streak on the warm side of the primary front. A rainband was observed with the primary front in both sections (band 2), although along the coast near the GLA profiler it did not exhibit convective characteristics, and its back edge rather than its forward edge coincided with the leading edge of the primary front aloft. The secondary cold-frontal analysis in each section was based on the same offshore P-3 data.<sup>2</sup>

Despite these similarities, key differences were observed that highlight the impact of the blocked flow on the primary cold front (Fig. 15). Most importantly, the airmass behind the primary front was unable to penetrate

<sup>2</sup> There were no nearshore P-3 measurements taken across the secondary cold front prior to the merging of this front with the remnant primary front (discussed in section 5b). However, because the nearshore P-3 measurements east of the secondary front at  $\sim 1235$  UTC match the prefrontal P-3 measurements taken offshore  $\sim 3$  h later, the offshore observations across the secondary front were included in the nearshore analysis.

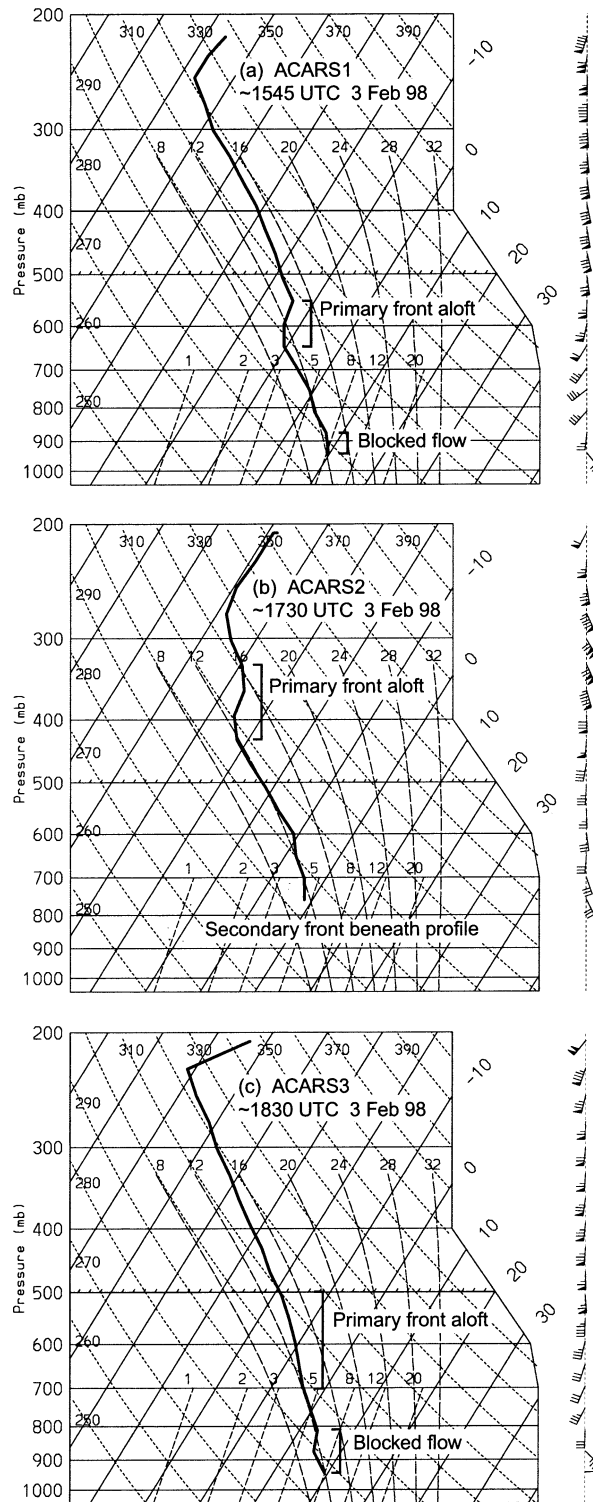


FIG. 14. Skew  $T$ -log $p$  soundings from ACARS commercial flight legs (shown in Figs. 12e,f) centered at (a) 1545, (b) 1730, and (c) 1830 UTC 3 Feb 1998. Wind flags and barbs are as in Fig. 2. Relevant meteorological features are labeled.

downward through the cooler blocked flow, quite likely because the stratification atop the blocked flow reduced the intensity of the vertical turbulent-scale mixing (Panoftsky and Dutton 1984). Hence, as the front advanced eastward beyond the western edge of the shallow blocked air mass, its lower terminus intersected the blocked air mass aloft rather than the ground, thus creating a cold front aloft. A numerical simulation of a California landfalling cold front by Doyle (1997) showed similar behavior as it encountered shallow blocked flow. Likewise, recent observational studies over the central United States (Neiman et al. 1998; Neiman and Wakimoto 1999) show cold fronts riding over potentially cooler, shallow air masses. The blocked flow caused the primary cold front to split in the vertical, thus taking on the appearance of a terrain-forced frontal occlusion. Bergeron (1937) referred to such a feature as a quasi-stationary orographic occlusion.

An important ramification of the frontal splitting is that the western edge of the blocked flow became the remnant low-level primary cold front, where a rainband (band 5) was observed (Fig. 15). To the west of this shallow front, postfrontal southwesterly flow prevailed, similar to that observed farther offshore. East of the front, the blocked air mass retained high values of  $\theta_e$ , resulting in an increase in low-level potential instability as the dry postfrontal air advanced eastward aloft. The blocked regime also contained strong southeasterly flow with a large barrier-parallel component below  $\sim 1$  km MSL. A prefrontal LLJ was situated east of the remnant low-level primary front, and it resulted in nonclassical wind shear characteristics through the primary cold front aloft near Vandenberg AFB (VNB) (Fig. 15). The LLJ intensity, its vertical position, and the reverse thermal gradient in which the LLJ was embedded were similar to what was observed away from the terrain (Fig. 7), thus suggesting that the LLJ remained dynamically tied to the lower-tropospheric portion of the primary cold front, even after it separated from its parent front aloft. Significantly, there was no evidence of an LLJ in the alongfront component in the blocked flow to the east of the cold front aloft. Observations from the Los Angeles (USC) profiler in the blocked flow (Fig. 16) also showed no evidence of an LLJ ahead of the primary cold front aloft. The frontal passage at USC occurred as a two-step transition between 1455 and 1545 UTC 3 February: 1) a shallow gust front ahead of the primary cold-frontal squall line (rain rate  $>32$  mm  $\text{h}^{-1}$ ), and 2) the trailing primary front aloft. The gust front was characterized by a sharp surface wind shift, a  $\theta$  decrease, and a pressure rise followed by a density-current head configuration in the isotachs below  $\sim 2$  km MSL, similar to thunderstorm outflow boundaries (Charba 1974; Goff 1976). The subsequent passage of the primary front above  $\sim 2$  km was marked by a wind shift from about  $27$  m  $\text{s}^{-1}$  southerly to about  $10$  to  $17$  m  $\text{s}^{-1}$  south-southwesterly flow. The weak ( $<10$  m  $\text{s}^{-1}$ ) post-gust

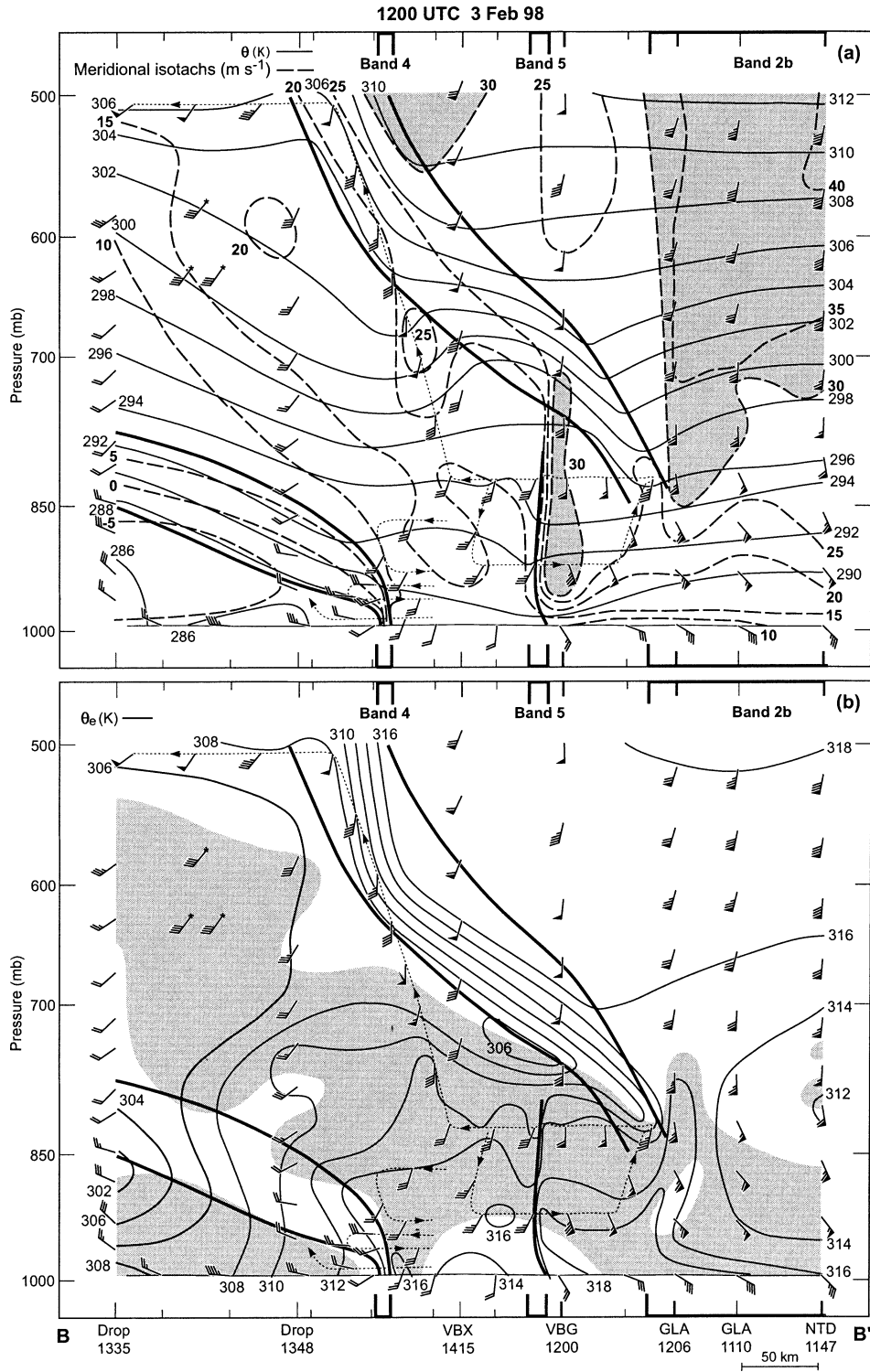


FIG. 15. Cross section of (a)  $\theta$  (K, solid) and meridional isotachs ( $\text{m s}^{-1}$ , dashed; shading  $>30 \text{ m s}^{-1}$ ), and (b)  $\theta_e$  (K) and potential instability (shaded), along line BB' in Fig. 12d at 1200 UTC 3 Feb 1998. Wind flags and bars are as in Fig. 2. Long vertical tick marks correspond to P-3 drosondes (Drop), rawinsondes (VBG, NTD, GLA), wind profiler data (GLA), and WSR-88D wind data (VBX); their deployment times (UTC) are shown. Short ticks are surface data. The nearshore P-3 flight track in the vicinity of the primary cold front between 1230 and 1335 UTC 3 Feb (ending near 500 mb) is depicted with a thin dotted line, as are portions of the offshore flight track near the secondary cold front between 1445 and 1605 UTC. Data have been time-to-space adjusted using a nearshore phase velocity of  $9.2 \text{ m s}^{-1}$  from  $270^\circ$ . Bold solid lines are frontal boundaries. The rainbands (heavy brackets top and bottom) are the same as in Figs. 6-9.

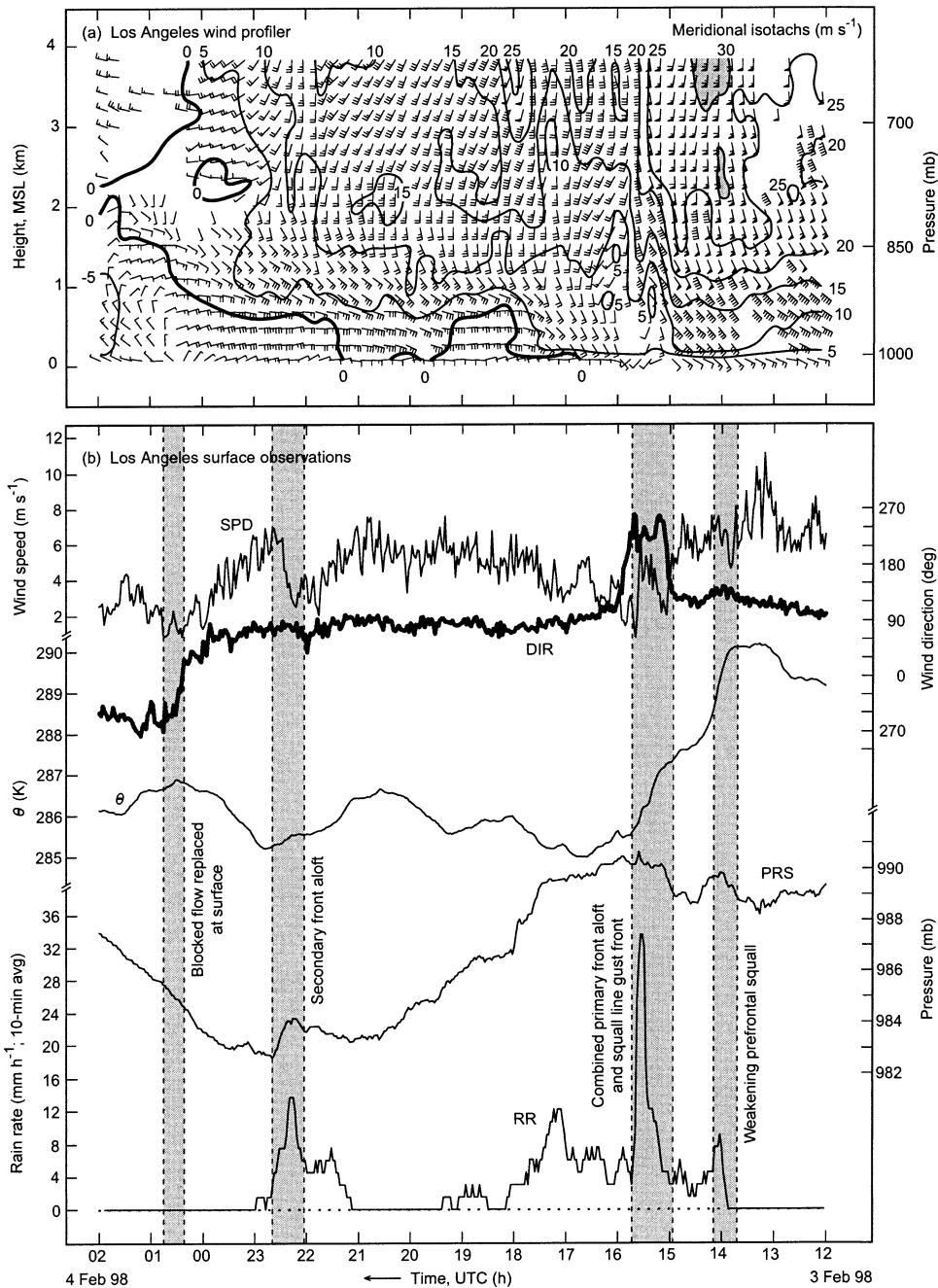


FIG. 16. Wind profiler and surface data from USC: (a) time-height section of 6-min wind profiles (flags and bars are as in Fig. 2) and meridional isotachs ( $m s^{-1}$ ; solid), and (b) time series of surface data [as in Fig. 8, except SPD = wind speed ( $m s^{-1}$ ) and DIR = wind direction (deg)]. The vertical gray-shaded bars bounded by dashed lines are as in Fig. 8.

front southerly flow below about 1 km reverted to blocked easterly after 1700 UTC.

Kinematic properties across the remnant low-level primary cold front were assessed using P-3 airborne radar observations taken during the lowest transect (shown in Fig. 15) through this front. Dual-Doppler analyses at 1 km MSL at 1234 UTC 3 February (Fig.

17; inset 1 in Fig. 12d) show the remnant primary front separating blocked and strong southeasterly flow to its east from weaker south to southwest flow to its west. The front was accompanied by a NCFR with cores exceeding 40 dBZ and by cyclonic relative vorticity ranging between about 10 and  $45 \times 10^{-4} s^{-1}$ . The vertical structure of this front is depicted along line CC' in Fig.

1234 UTC 3 February 1998; 1.0 km, MSL

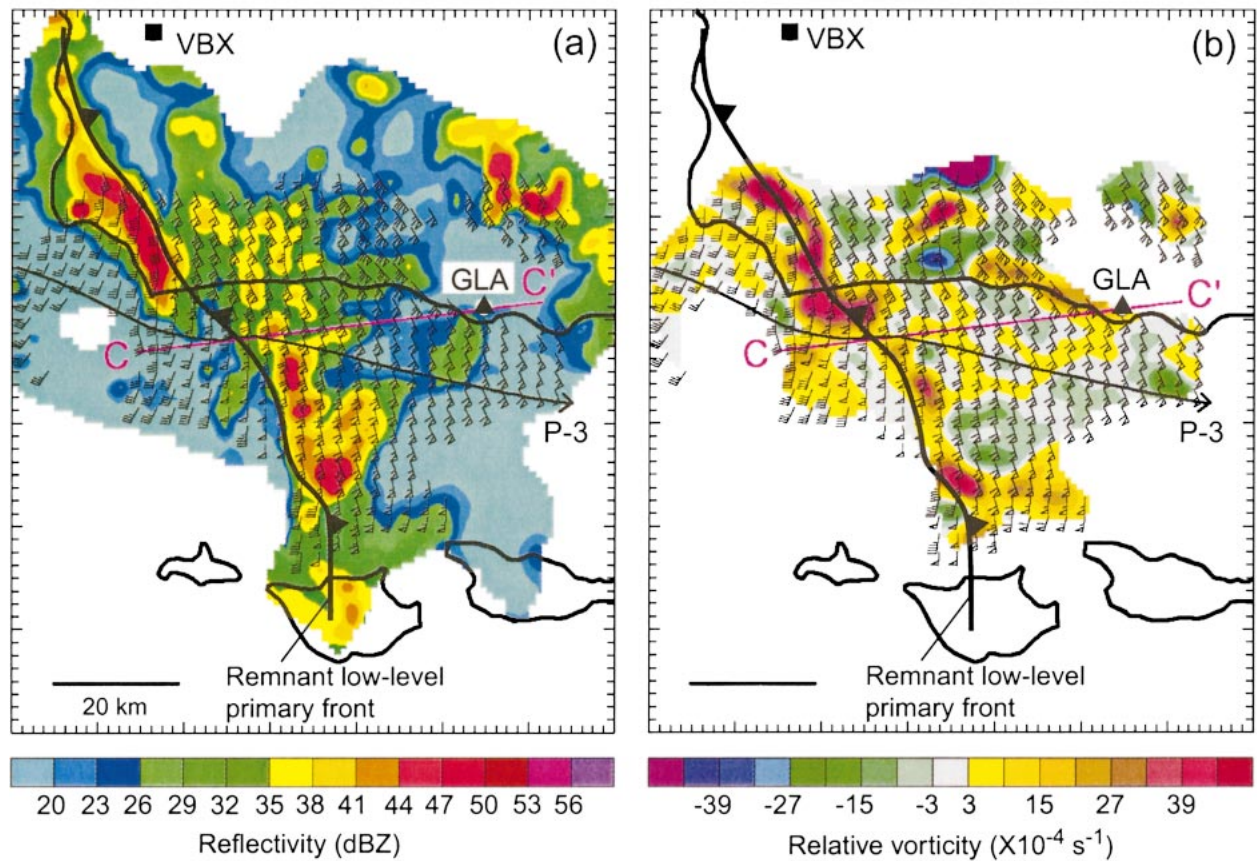


FIG. 17. Airborne dual-Doppler radar analysis from the P-3 aircraft at 1 km MSL at 1234 UTC 3 Feb 1998: (a) reflectivity (dBZ) and horizontal wind velocities, and (b) relative vorticity ( $\times 10^{-4} \text{ s}^{-1}$ ) and horizontal wind velocities. Wind flags and barbs, and the frontal notation, are as in Fig. 2. Line CC' is a cross-section projection for Fig. 18. The P-3 flight track is marked as a thin black line.

17. The cross section of reflectivity and section-parallel wind vectors (Fig. 18a) shows a 3-km-deep NCFR embedded within a  $1\text{--}2 \text{ m s}^{-1}$  updraft. Strong barrier-jet inflow below about 1 km on the east side of the shallow front impinged upon the postfrontal westerly component flow, resulting in frontal convergence ( $\sim 25 \times 10^{-4} \text{ s}^{-1}$ ) that triggered the convection. By considering the theoretical results of Rotunno et al. (1988) that describe the relationship between the horizontal vorticity balance and the character of lifting within long-lived squall lines, it is likely that the barrier jet contributed to the NCFR's forward tilt, because this jet created stronger cross-frontal vertical shear in the prefrontal environment than did the cold pool west of the front. Recent findings by Jorgensen et al. (2003) demonstrate the applicability of the Rotunno et al. theory in explaining alongfront variations in the vertical structure of a maritime NCFR.

A companion radar cross section of wind profiles and alongfront isotachs (Fig. 18b) further highlights the splitting of the primary cold front. An axis of maximum thermal wind-derived cold advection marked the primary front aloft at about 5 km MSL. Beneath this directional shear layer, postfrontal southwesterly flow cen-

tered at about 3 km MSL was observed above GLA, though it did not penetrate downward to the surface here due to the shallow blocked southeasterly flow. However, the postfrontal southwesterly flow did descend to the surface west of the remnant low-level primary front, where a shallow cold-air-advection signature at about 2 km MSL was observed. This two-tiered, cold advection signature reflected the cold-frontal splitting by the blocked flow. The top of this blocked flow exhibited strong clockwise turning of the wind with height (maximized along the dotted line) between 1.0 and 1.5 km MSL (see also Fig. 11b). The prefrontal LLJ was cradled between the top of the blocked flow and the remnant low-level front. Because the LLJ was situated above the blocked flow and oriented perpendicular to the downstream barrier, it is likely that the LLJ was dynamically driven primarily by the low-level frontal circulation rather than by the blocked flow.

## 2) SECONDARY COLD FRONT

Blocking farther east across the Los Angeles Basin resulted in the vertical splitting of the secondary cold

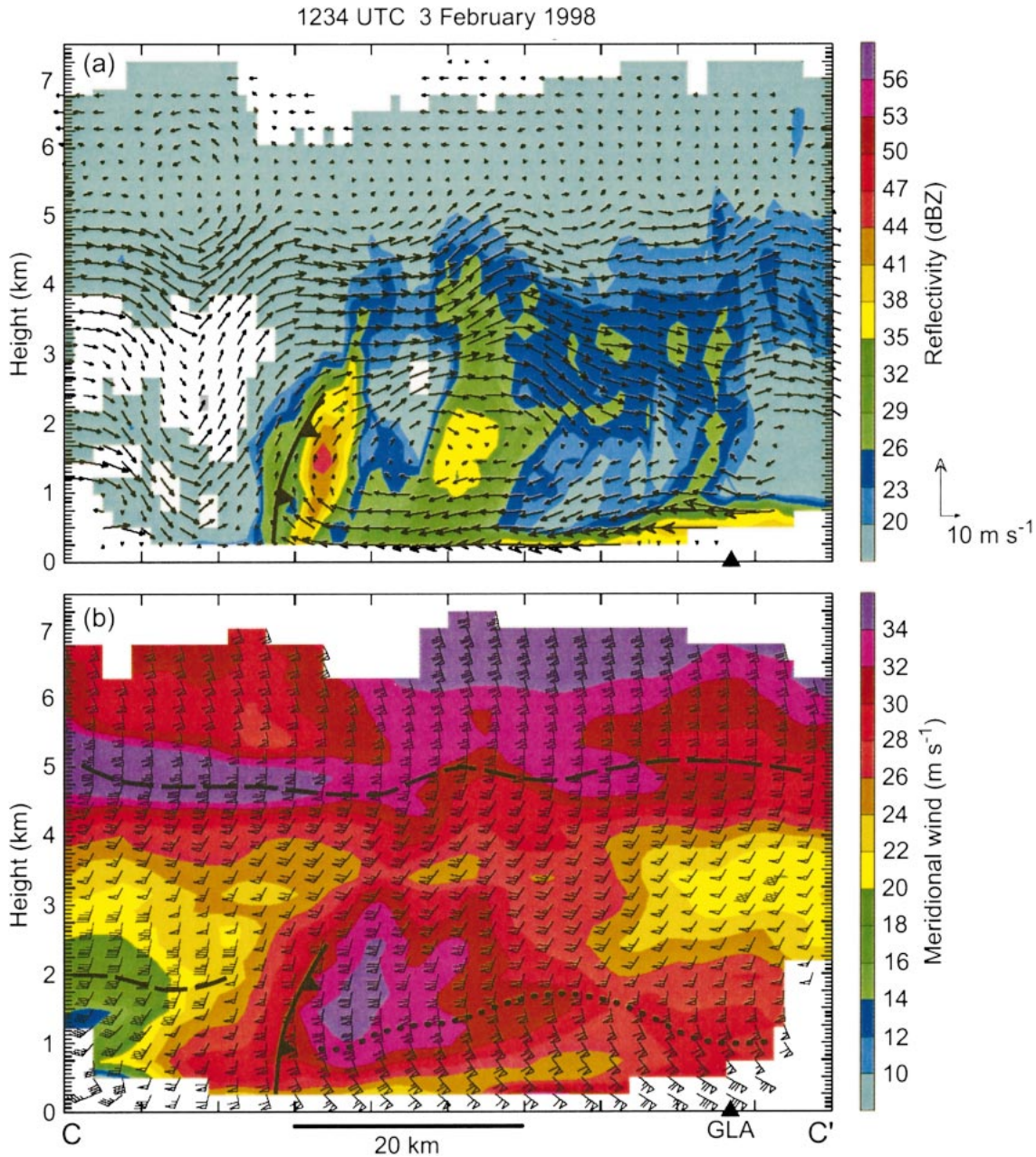


FIG. 18. Airborne dual-Doppler radar cross-section from the P-3 aircraft along line CC' in Fig. 17: (a) reflectivity (dBZ) and ground-relative wind vectors in the plane of the section (scale on right), and (b) meridional isotachs ( $\text{m s}^{-1}$ ) and horizontal wind velocities. Wind flags and barbs, and the frontal notation, are as in Fig. 2. The bold dashed and dotted lines in (b) mark the axes of maximum thermal wind-derived cold and warm advection, respectively. The profiler site at GLA is shown.

front there, where the blocked flow below 925 mb was at least as cold ( $\theta \leq \sim 287$  K) as the air mass immediately behind the secondary front. The USC profiler observed deepening blocked easterlies after 1700 UTC 3 February (Fig. 16), whereas ambient postprimary-frontal southwesterly flow was observed aloft. The secondary front moved across USC between 2200 and 2240 UTC above 2 km MSL when winds shifted from south-

erly to westerly during a period of enhanced rainfall. Thereafter, surface pressure increased steadily, marking the change in air masses aloft. Because the  $\theta$  behind the advancing secondary cold front decreased westward to  $< 286$  K (Fig. 15a), this postfrontal air mass eventually became colder than the blocked air mass over Los Angeles, thus replacing it. The low-level shift to northwesterly flow and the initial decrease in surface  $\theta$  after

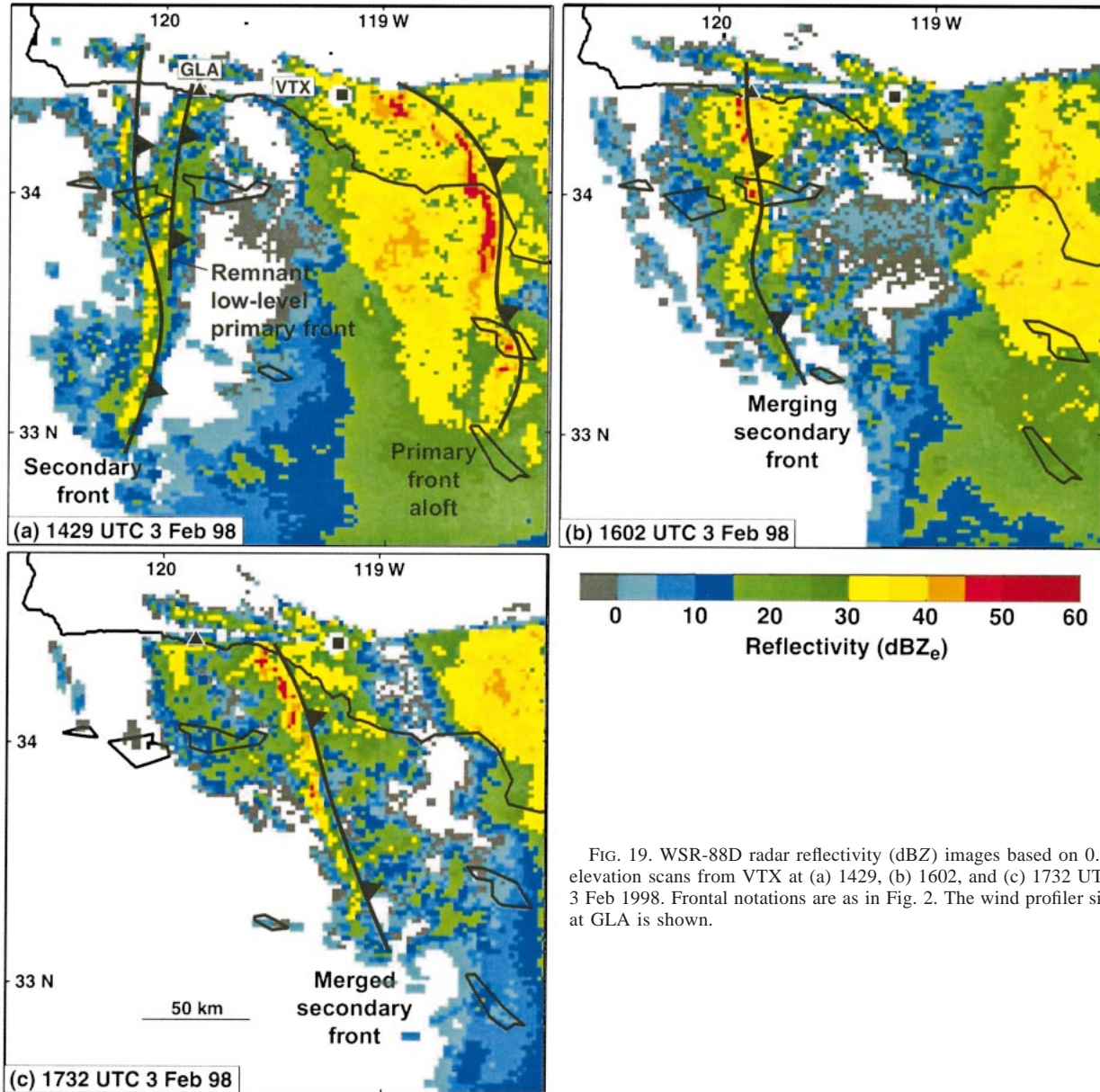


FIG. 19. WSR-88D radar reflectivity (dBZ) images based on 0.5° elevation scans from VTX at (a) 1429, (b) 1602, and (c) 1732 UTC 3 Feb 1998. Frontal notations are as in Fig. 2. The wind profiler site at GLA is shown.

0020 UTC 4 February (Fig. 16) marked the onset of this transition from blocked to postfrontal conditions.

*b. Frontal merging*

Because the  $\theta$  within the shallow blocked air mass increased westward along the north coast of the Bight (Fig. 13), the western portion of the blocked air mass was warmer than the air mass behind the advancing secondary cold front. As a result, the secondary front displaced the blocked flow to the east of the nearly stationary remnant low-level primary front near GLA. Alternately stated, blocking led to the merging of the secondary front with the remnant primary front which,

in turn, profoundly impacted the secondary cold-frontal dynamics and precipitation. This section quantitatively explores the modification of the secondary front by this blocking-induced merger.

The secondary cold front exhibited weak and shallow-sloping characteristics offshore (Fig. 15) prior to its merger with the remnant primary front to the east. Weak multibanded precipitation observed by the WSR-88D radars accompanied the secondary front as it approached the coast between 1230 and 1335 UTC 3 February (Figs. 9c–d). Beyond the range of these radars, the P-3 observed a weak rainband with the secondary front in the unblocked flow over the central Bight (Fig. 6). The WSR-88D radar at Ventura (VTX) captured the precip-

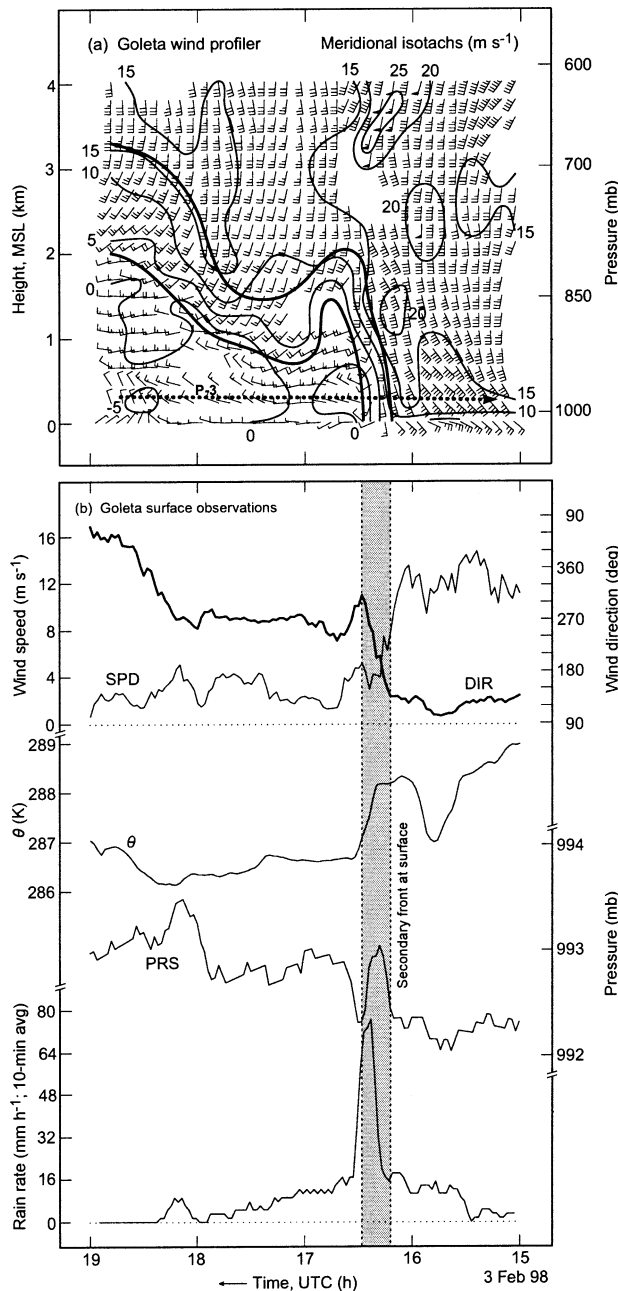


FIG. 20. Wind profiler and surface data from GLA: (a) time-height section of 6-min wind profiles (flags and barbs are as in Fig. 2) and meridional isotachs ( $\text{m s}^{-1}$ ; solid), and (b) time series of surface data (as in Fig. 16). Bold lines in (a) portray frontal boundaries; (a) contains a time-height representation of a nearby P-3 flight leg (bold dotted line; see also Fig. 21a).

itation evolution during the frontal merger across the northern Bight (Fig. 19). At 1429 UTC, a rainband with the secondary front was approaching the weakening rainband along the remnant primary front west of the GLA profiler. By 1602 UTC, the precipitation along the merging secondary front was intensifying to the west

and southwest of GLA. At 1732 UTC, a mature squall line accompanied the merged secondary front.

The secondary front evolved from a shallow-sloping boundary offshore (Fig. 15) to a nearly upright feature at GLA (Fig. 20a) following its merger with the remnant low-level primary front. Intense convective precipitation, which accompanied the merged frontal passage at GLA ( $77 \text{ mm h}^{-1}$ ; Fig. 20b), quite likely contributed to the front's upright character (Browning and Harrold 1970). Although the postfrontal west-northwesterly flow behind the secondary front was similar offshore and at the coast (i.e., before and after merging; Figs. 15 and 20, respectively), the prefrontal flow conditions were markedly different. Namely,  $14\text{--}18 \text{ m s}^{-1}$  south-southwesterly flow characterized the prefrontal environment below 900 mb offshore (Fig. 15), whereas  $15\text{--}20 \text{ m s}^{-1}$  southeasterly flow was observed in the prefrontal air mass in the blocked flow along the coast (Fig. 20). Surface traces at GLA reveal that the frontal transition and postfrontal air mass extended downward to the surface.

The P-3 penetrated the merged secondary front offshore of GLA at 290 m MSL (Fig. 21a), where a sharp wind shift was observed. The 1-s aircraft data (Fig. 21b) reveals an abrupt 6.4-km frontal transition from  $14 \text{ m s}^{-1}$  west-northwesterly flow to  $19 \text{ m s}^{-1}$  blocked southeasterly flow. The front-normal wind component, which is approximated by the zonal component of the flow given the north-south frontal orientation, decreased from  $13.8$  to  $-11.8 \text{ m s}^{-1}$ . Hence, assuming two-dimensionality, the cross-frontal convergence at 290 m MSL was  $40 \times 10^{-4} \text{ s}^{-1}$ . The  $\theta_e$  trace increased from 310 K in the postfrontal air mass to 317.5 K in the moisture-rich blocked flow to the east, while the  $\theta$  increased from 287 to 289.5 K (not shown). A 0.75-mb pressure jump and a  $\pm 3$  to  $4 \text{ m s}^{-1}$  vertical motion couplet near the forward edge of the front coincided with the squall line.

Comparison of this flight leg with an offshore transect through the same front at the same altitude  $\sim 75$  min earlier provides insight into the squall line development during the frontal merger. The offshore transect, which corresponds to the second-to-lowest flight leg through the unmerged secondary front in Fig. 15, measured postfrontal west-northwesterly flow with a zonal component of about  $14.5 \text{ m s}^{-1}$ . This value is very similar to that observed behind the merged secondary front farther north. In contrast, prior to the merger the unblocked prefrontal south-southwesterly flow offshore exhibited a westerly component of  $6.9 \text{ m s}^{-1}$ , whereas after the merger the prefrontal southeasterly flow along the coast possessed a significant easterly component of  $-11.8 \text{ m s}^{-1}$  due to the blocking. In addition, the cross-frontal width was 4.4 times larger in the unmerged state offshore than after the merger along the coast, thus yielding low-level cross-frontal convergence of  $3 \times 10^{-4} \text{ s}^{-1}$  offshore. Based on the zonal wind measurements across the secondary front offshore and along the coast, the low-level cross-frontal convergence increased by more

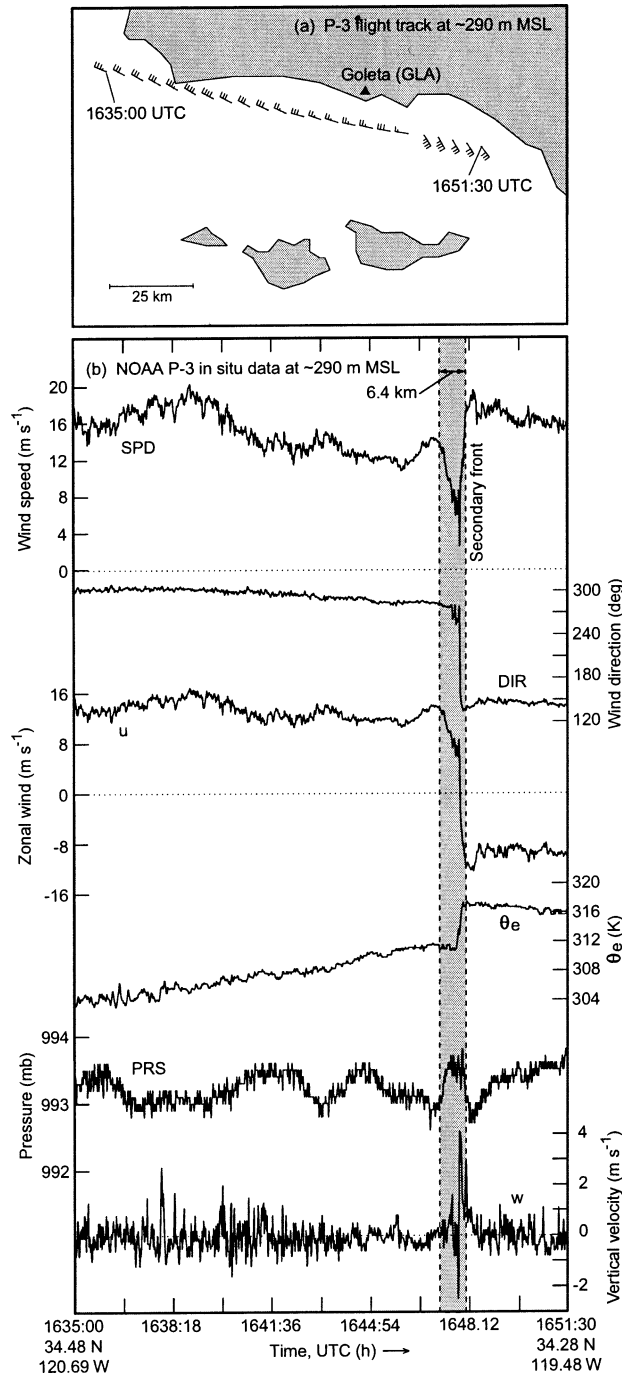


FIG. 21. (a) The P-3 flight leg at about 290 m MSL between 1635:00 and 1651:30 UTC 3 Feb 1998, with selected wind flags and barbs (as in Fig. 2). (b) Time series of flight-level data along the track shown in (a) [as in Fig. 16, except  $u$  = zonal wind ( $\text{m s}^{-1}$ );  $\theta_e$  = equivalent potential temperature (K);  $w$  = vertical velocity ( $\text{m s}^{-1}$ )]. The gray-shaded bar in (b) denotes the frontal transition at about 290 m MSL. This flight leg was placed on Fig. 20a for context.

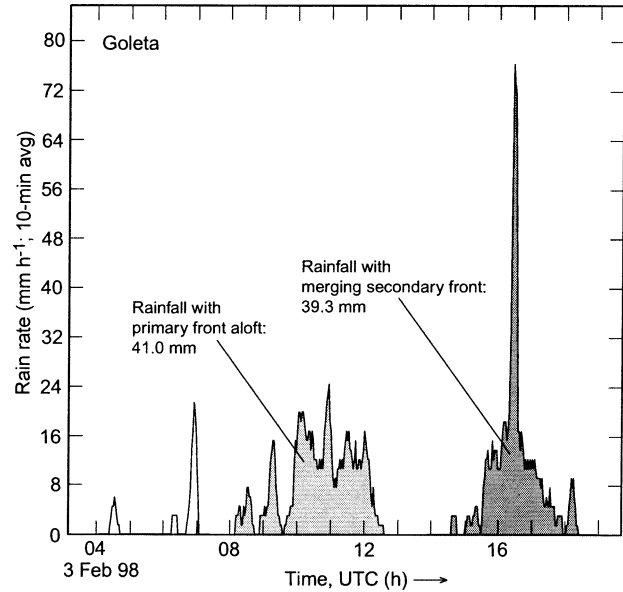


FIG. 22. Time series of rain rate ( $\text{mm h}^{-1}$ ; 10-min averaging period) from GLA. Light and medium shading under the curve correspond to the rainfall associated with the primary front aloft and the merging secondary front, respectively. Total rainfall for these two periods are shown.

than an order of magnitude after the secondary front merged with the remnant low-level primary front. The enhanced convergence resulted from the maintenance of easterly component flow in the blocked prefrontal airstream and the frontal-scale collapse during the merging process. The prefrontal airstream had higher values of  $\theta_e$  in the blocked flow along the coast ( $\sim 317.5$  K) than in the unblocked flow offshore (316.0 K), hence, this airstream was potentially more unstable following the frontal merger.

Based on the above flight-leg comparison, the merger of the secondary front with the remnant primary front significantly enhanced the low-level frontal convergence (i.e., forced ascent), which then acted upon the blocked prefrontal air mass that possessed higher values of  $\theta_e$  and greater potential instability than what was observed offshore in the unblocked prefrontal airstream prior to merging. Hence, the frontal merger resulted in an overlapping set of conditions that favored the development of significant convection. The secondary cold-frontal squall line generated a peak rainrate of  $77 \text{ mm h}^{-1}$  at GLA, 3 times larger than that observed with the passage of the primary cold front aloft (Fig. 22) and more than twice as large as that observed with the passage of the mature primary cold-frontal squall line at SCE and USC (Figs. 8, 16). In fact, this extreme rainrate was the largest observed anywhere in southern California during this event. This squall line contributed significantly to the 39.3 mm of rain that fell at GLA during the secondary frontal passage, which is comparable to the 41.0 mm of rain that fell during the passage of the primary cold front aloft (Fig. 22). The rain

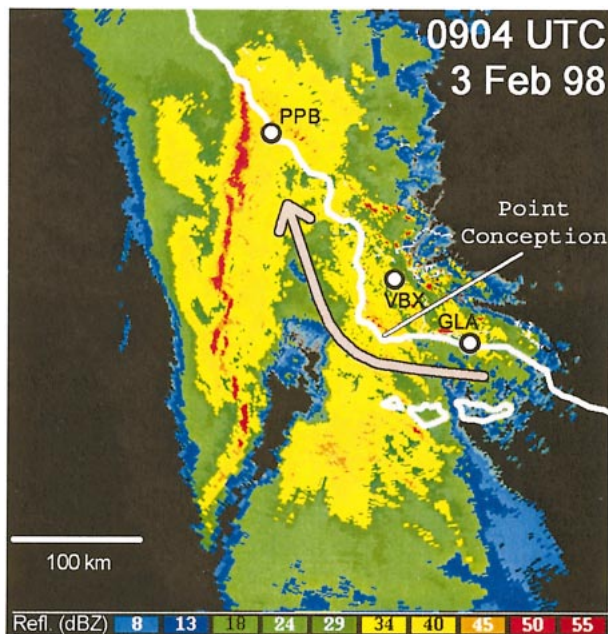


FIG. 23. WSR-88D radar reflectivity (dBZ) image based on a  $0.5^\circ$  elevation scan from VBX at 0904 UTC 3 Feb 1998. The low-level blocked flow is portrayed as a bold arrow. The wind profiler sites at GLA and PPB are shown.

with the primary front aloft saturated the soil, while the blocking-induced convective rain with the merged secondary cold front fell on the saturated soil and resulted in flash flooding.

### c. Frontal waves

Blocking initially disrupted the eastward advance of the primary cold front and its NCFR west of the California Bight. A representative image from the Vandenberg AFB radar (VBX; Fig. 23) shows the retardation of the NCFR by the shallow blocked flow rounding Point Conception. The resulting wedgelike region formed by the NCFR and coastline is similar to that observed farther north in the coastal zone (Doyle 1997; Braun et al. 1997; Yu and Smull 2000; Yu and Bond 2002). Numerical results by Doyle (1997) reveal that low-level blocking can force a nearshore rainband to emulate a wedge-shaped structure around a coastal jet that is dynamically trapped between the coastal orography and the impinging cold front. Similarly, idealized results by Braun et al. (1997) show the upstream influence of coastal orography and blocking on the nearshore orientation of a landfalling cold-frontal rainband.

The fortuitous siting of the VBX radar also yielded unique documentation of the NCFR evolving into a pair of waves along the remnant low-level primary front at the western periphery of the blocked flow. The frontal-wave evolution exhibited four phases (Fig. 24): incipient, mature, late mature, and dissipative. During the incipient phase (Fig. 24a), the NCFR initially tracked

eastward as a quasi-linear feature with the vertically coherent primary cold front. Between 0817 and 1015 UTC, however, two frontal waves were forming to the west of the region where the blocked easterly flow along the north shore of the Bight rounded Point Conception and migrated northwestward along the coastal zone. Wind profiler observations from PPB (not shown) captured the onset of frontal splitting during this period, with the cold front aloft moving across the profiler some 35 min earlier than at the surface. The mature phase (Fig. 24b) was characterized by the two well-defined waves along the remnant low-level primary front. These waves had a wavelength of about 125 km and were therefore larger than NCFR gap-core instabilities, which have wavelengths of 20–80 km (James and Browning 1979; Hobbs and Persson 1982; Locatelli et al. 1995; Wakimoto and Bosart 2000). The southern wave persisted along the remnant front during the late mature phase (Fig. 24c), when the primary cold front aloft was about 75 km farther east (Figs. 12d, 15). The precipitation organization with the southern wave became less coherent as it made landfall in the orographically complex region near Point Conception. This organization degraded further during the dissipative phase (Fig. 24d).

Time series of in situ data from PPB, four buoys, and the P-3 (locations shown in Fig. 24) reveal that the frontal waves possessed classical signatures typical of larger-scale frontal waves. The initial passage of the remnant low-level primary front at PPB at 0952 UTC (Fig. 25a) was characterized by a cold-frontal transition from strong ( $18\text{--}22\text{ m s}^{-1}$ ) southeasterly winds within the high- $\theta_e$  (317 K) blocked prefrontal airstream to weaker and cooler postfrontal south-southwesterly flow. As the northern wave developed and propagated downstream, the front then moved northward across PPB as a warm front at about 1100 UTC, followed by the return of strong southeasterly prefrontal flow of high- $\theta_e$  air. These warm-sector conditions persisted until about 1135 UTC, when the remnant front passed PPB for a third time, as a cold front again. Thereafter, conditions reverted to a southerly postfrontal regime until the passage of the secondary cold front at about 1330 UTC. Farther south, similar behavior was observed with 10-min wind data at buoy 46062 during the passage of the southern-wave warm sector (Fig. 25b). The three remaining buoys were situated south of the transient frontal waves, hence, they each observed only a single transition associated with the passage of the remnant front (Figs. 25c–25e). The P-3 flew through the southern wave warm sector at 822 mb between 1215 and 1223 UTC (Fig. 25f), where it encountered strong southerly component flow and large values of  $\theta_e$  in the prefrontal airstream. At about 1238 UTC, the aircraft again penetrated the remnant front, this time at 919 mb. Strong southeasterly flow with high- $\theta_e$  content was again observed in the blocked prefrontal airstream on the warm side of the front. This latter penetration is shown in Fig. 17.

The P-3 radar observations taken through the south-

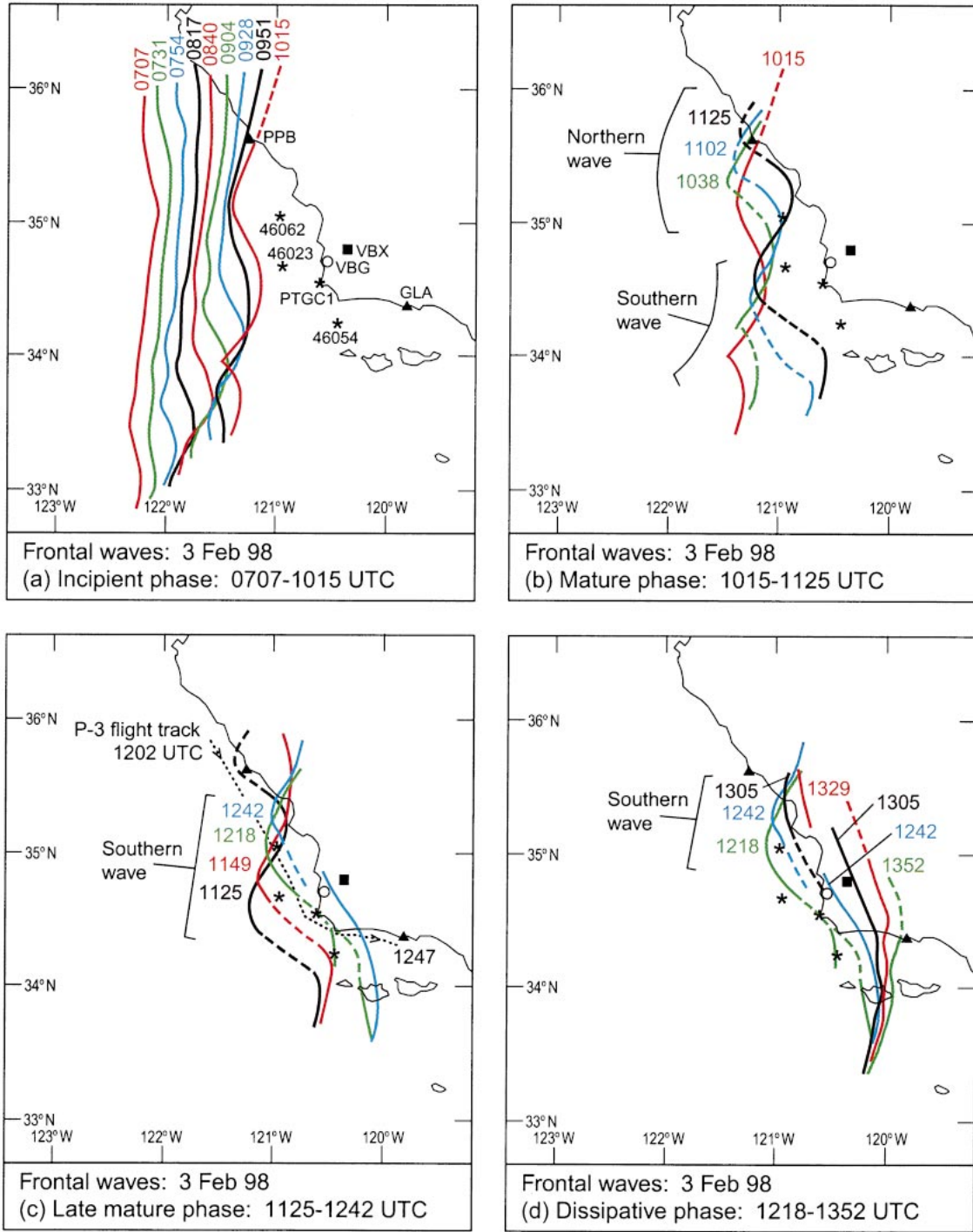


FIG. 24. Isochrone analysis of the rainband associated with the remnant low-level primary front during four phases of frontal wave development on 3 Feb 1998 as observed by the 0.5° elevation radar scans at VBX: (a) incipient phase, 0707–1015 UTC, (b) mature phase, 1015–1125 UTC, (c) late mature phase, 1125–1242 UTC, and (d) dissipative phase, 1218–1352 UTC. Solid and dashed isochrones indicate solid and broken segments of the rainband, respectively. The sites of relevant observing systems are marked on each panel (■ = WSR-88D radar; ▲ = wind profilers; ○ = rawinsonde; \* = 10-min-resolution buoys); their station call letters are shown in (a). The P-3 flight track between 1202 and 1247 UTC 3 Feb is depicted with a thin dotted line in (c).

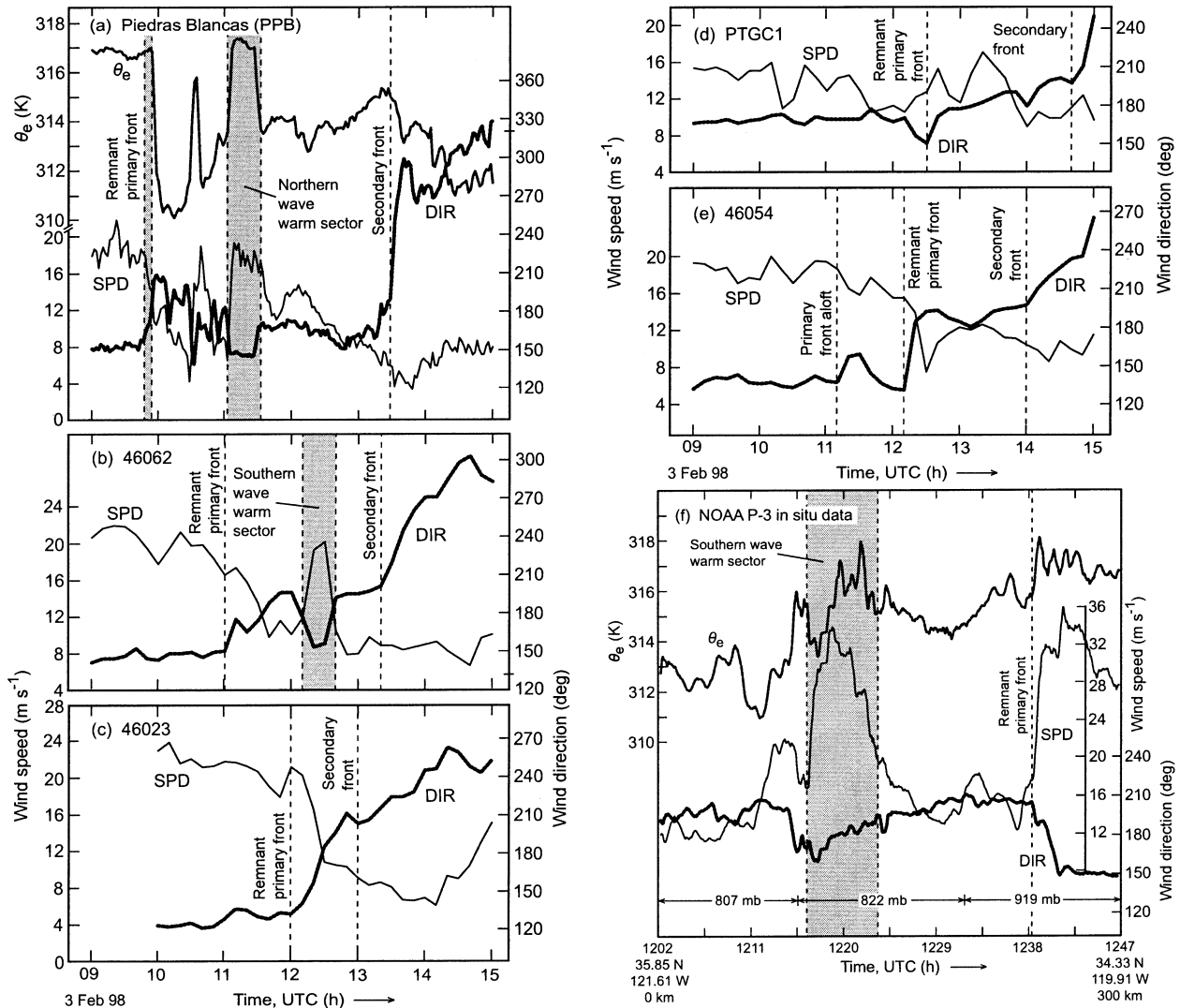


FIG. 25. Time series of (a)–(e) surface data between 0900 and 1500 UTC 3 Feb 1998 from selected observing sites (see Fig. 24a), and (f) flight-level data between 1202 and 1247 UTC (see Fig. 24c for flight track). Time series are as in Fig. 21b. Vertical dashed lines and gray-shaded bars mark relevant transitions.

ern frontal wave yielded a three-dimensional kinematic depiction of the wave environment. A dual-Doppler analysis at 1 km MSL at 1155 UTC 3 February (Fig. 26; inset 2 in Fig. 12d) shows the remnant low-level primary front separating strong south-southeasterly flow in the warm sector from weaker south-to-southwest flow to its west. Broken-line convection coincided with the southern portion of the front, and continuous precipitation accompanied the northern portion. The asymmetric distribution of precipitation along the front is attributable to the reorientation of the front by the frontal wave evolution. Specifically, the strong southerly component warm-sector flow impinged upon the weaker southerly component flow situated north of the southwest–northeast-oriented warm front, resulting in strong low-level frontal convergence ( $\sim 45 \times 10^{-4} \text{ s}^{-1}$ ; not shown) in the vicinity of the widespread precipitation.

Conversely, low-level convergence was nearly nonexistent along the southern portion of the front that was aligned northwest–southeast with the broken-line convection, because the cross-front component of the warm-sector flow was at least as large as within the weaker cool sector flow farther to the south.

A radar cross section through the remnant front along DD' (Fig. 27a) shows a shallow, well-defined cross-frontal gradient of meridional flow collocated with the NCFR, where an updraft of about  $1.4 \text{ m s}^{-1}$  was observed below 1.3 km MSL (not shown). This section contains the same two-tiered cold advection signature that was observed in the north Bight region (Fig. 18b), thus highlighting the vertical splitting of the primary cold front by the shallow blocked flow upcoast of the California Bight. Due to the frontal splitting, the fast flow aloft decoupled from the strong low-level blocked

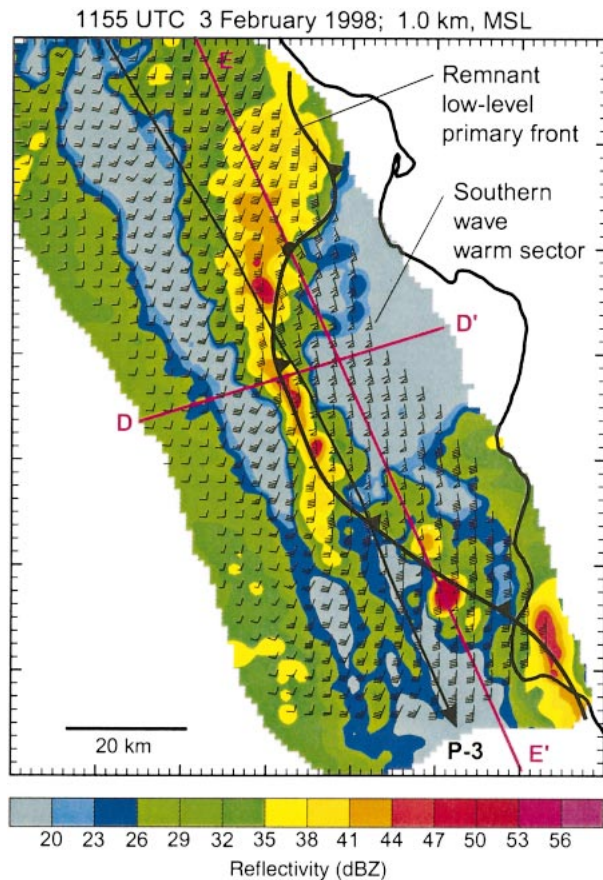


FIG. 26. Airborne dual-Doppler radar analysis of reflectivity (dBZ) and horizontal wind velocities from the P-3 aircraft at 1 km MSL at 1155 UTC 3 Feb 1998. Wind flags and barbs, and the frontal notation, are as in Fig. 2. Lines DD' and EE' are cross-section projections for Figs. 27a and 27b, respectively. The P-3 flight track is marked as a thin black line.

flow ahead of the remnant front; this decoupling occurred slightly above the 1.5-km coastal terrain. A prefrontal southerly LLJ centered at about 1.3 km extended up to nearly 3 km on the warm side of the remnant front, while secondary jet maxima with an easterly component resided farther east and closer to the ocean surface within the blocked flow. The horizontal segment of the warm-advection signature east of the remnant front marked the ageostrophic vertical shear through the blocked flow, while its ascending branch quite likely represented “true” warm advection immediately ahead of the front within the prefrontal LLJ. The core of this LLJ resided at the altitude of the shear layer capping the blocked flow, as was also the case about 40 min later along the north shore of the Bight (Fig. 18b).

A cross section through the southern frontal wave along EE' (Fig. 27b) also captured the prefrontal LLJ in the warm sector at the top of the blocked flow, as well as the vertical splitting of the primary cold front. Because this section sliced through the wave in its entirety, it shows the warm sector flanked on both sides

by the remnant low-level front and weaker cool-sector flow, though the southern and northern portions of the remnant front exhibited fundamentally different characteristics. Namely, the southern portion was accompanied by two shallow convective plumes in the vicinity of weak frontal convergence and ascent ( $10 \times 10^{-4} \text{ s}^{-1}$  and  $1 \text{ m s}^{-1}$ , respectively; not shown). Here, the front was migrating northeastward as a cold front. In contrast, the northern portion was accompanied by widespread and deeper precipitation embedded within strong convergence and ascent ( $40 \times 10^{-4} \text{ s}^{-1}$  and  $3\text{--}6 \text{ m s}^{-1}$ , respectively; not shown). Based on the analysis of two-dimensional wind vectors in the plane of the section (not shown), the ascent was organized into a deep slantwise plume that tracked closely with the sloping layer of warm advection and entrained the strong southeasterly blocked flow of high- $\theta_e$  air into the middle troposphere. These warm-frontal characteristics resulted from the local reorientation of the remnant low-level front during the frontal wave development.

The frontal waves not only had a major impact on the redistribution of precipitation offshore, but also along the coast. This is illustrated by inspecting measurements from six rain gauges in and near the Santa Lucia Mountains (Table 1). During the incipient phase of frontal wave development, the NCFR initially migrated eastward across the gauges in the Santa Lucia Mountains and at the PPB profiler at the coast (Fig. 24a). Then, the NCFR stalled and subsequently shifted northward with the approach of the northern frontal wave (Fig. 24b). Table 1 summarizes the rainfall with the NCFR (defined by a rain rate  $>12 \text{ mm h}^{-1}$ ) and during the 21-h storm period at each site. The four northern mountain gauges recorded a NCFR duration of 30–45 min, and the NCFR rainfall at these sites represented 10%–18% of the storm total. At these sites, the NCFR motion was not affected by the frontal waves. In contrast, the two southern sites were significantly impacted by the oscillatory motion of the NCFR associated with the northern wave. Here, the NCFR rainfall, which persisted for 60–150 min, represented 35%–36% of the storm total. As a result, the average ratio of NCFR rainfall to storm-total rainfall was almost 3 times larger in the region influenced by the northern wave. These observations establish that the northern wave enhanced the already heavy rainfall at the southern end of the Santa Lucias (see Fig. 5), resulting in extreme flooding there (NCDC 1998).

The similarity in shape and scale between the waves along the remnant low-level primary front and the bend in the coastline near Point Conception suggests that blocking played an integral role in the wave development. We hypothesize that the blocking contributed to the wave development in a two-step process. First, the influence of blocking along the primary front was inhomogeneous due to the acute angle between the front and shoreline. Hence, the northern portion of the front was retarded earlier than the southern portion, thus pro-

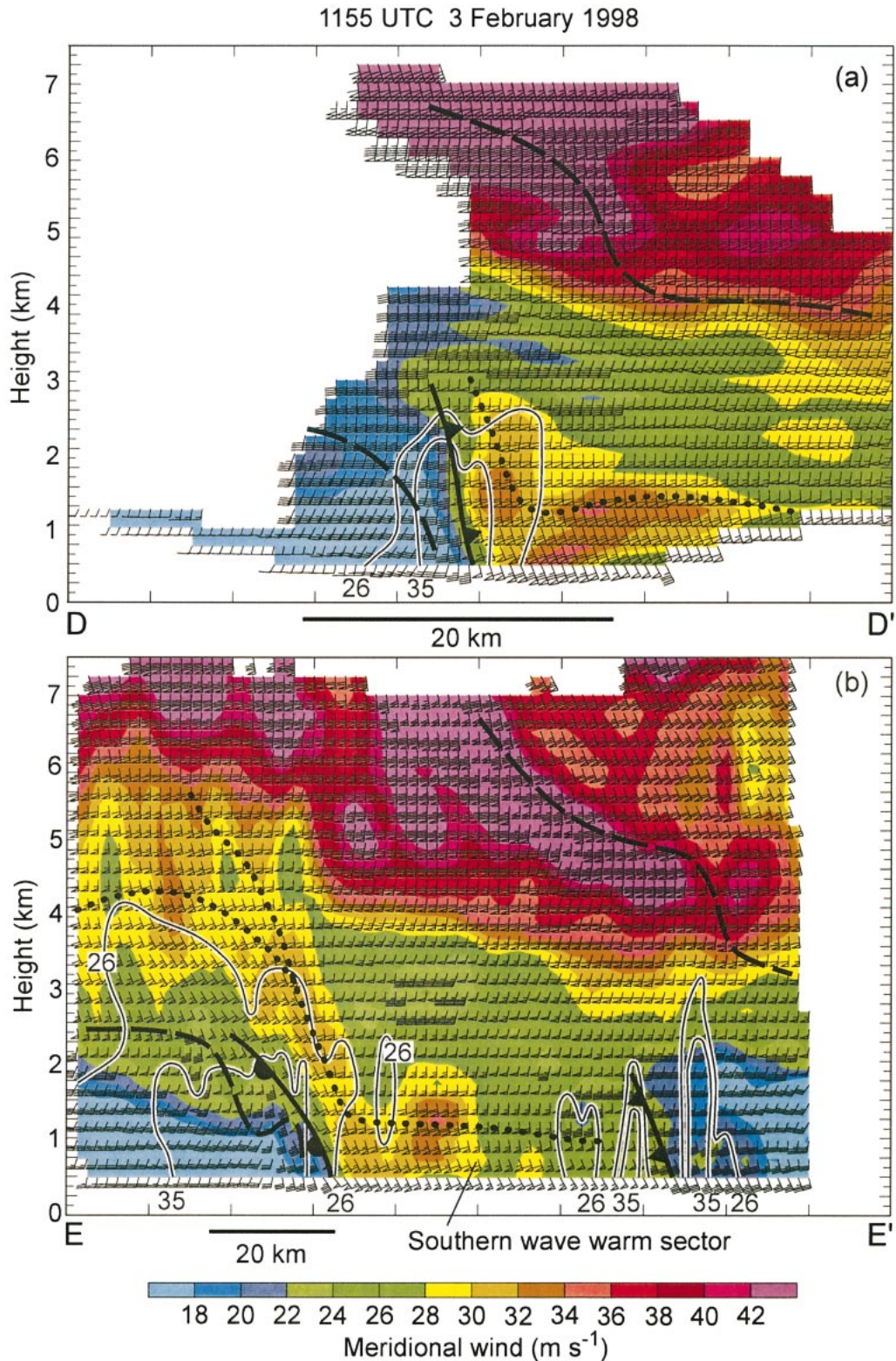


FIG. 27. Airborne dual-Doppler radar cross-section of meridional isotachs ( $\text{m s}^{-1}$ ) and horizontal wind velocities from the P-3 aircraft along lines (a) DD' and (b) EE' in Fig. 26. Wind flags and barbs, and the frontal notation, are as in Fig. 2. The 26- and 35-dBZ reflectivity contours (thin solid) are shown. The bold dashed and dotted lines are as in Fig. 18b.

TABLE 1. Rainfall characteristics at selected sites in and near the Santa Lucia Mountains during the landfall of the winter storm and its NCFR on 3 Feb 1998. The NCFR is defined by a rain rate exceeding  $12 \text{ mm h}^{-1}$  during the primary cold-frontal passage. The five rain gauges in the mountains recorded data every 15 min, and the temporal resolution of the 2-min rain gauge data at PPB was degraded to match the resolution at the mountain sites. The locations of these six sites are shown in Fig. 1.

Station (see Fig. 1 for locations)	Elev (m)	NCFR start time (UTC)	NCFR end time (UTC)	NCFR duration (min)	Total NCFR rainfall (mm)	21-h rainfall total* (mm)	Ratio of NCFR rainfall to total rainfall	Avg ratio of NCFR rainfall to total rainfall
WRR	1050	0800	0845	45	13.0	99.0	0.13	
VTC	1448	0830	0900	30	9.9	101.3	0.10	Before NCFR
ANP	1158	0800	0845	45	13.0	72.1	0.18	Stalled: 0.128
MNR	1436	0830	0900	30	14.2	148.8	0.10	
TPK	1021	0900	1130	150	81.0	224.8	0.36	After NCFR
PPB	11	1000	1100	60	25.5	73.8	0.35	Stalled: 0.355

\* The 21-h rainfall total is valid for the same time window as was used for the rainfall analysis in Fig. 5, that is, between 0000 and 2100 UTC 3 Feb 1998.

ducing wavelike kinks. Second, blocking resulted in the vertical splitting of the primary front and its large-scale frontogenetic stretching deformation (i.e., “strain”). Theoretical studies by Dritschel et al. (1991) and Bishop and Thorpe (1994a,b) show that the large-scale strain associated with a front plays a key role in the evolution of barotropic waves along that front. Sufficiently intense large-scale strain flow will suppress low-level barotropic wave development in a region of strong cross-front shear, because the waves are compressed in the cross-front direction. If the large-scale strain weakens significantly, however, barotropic wave development is no longer constrained along that front. This theoretical relationship was verified quantitatively with analyzed cases of secondary frontal wave development over the North Atlantic (Renfrew et al. 1997; Chaboureaud and Thorpe 1999), and it may also explain that, in our case, the blocking-induced change of the large-scale strain was favorable for the wave development along the remnant low-level front. Namely, prior to encountering the blocked flow, the advancing primary cold front was vertically continuous, such that the large-scale strain tracked with the low-level portion of the front and inhibited barotropic frontal wave development (note the quasi-linear NCFR before 0800 UTC 3 February in Fig. 24a). After the front impinged on the blocked flow, the large-scale strain advanced eastward with the front aloft, while the remnant low-level portion of the front remained fixed at the western periphery of the blocked flow, where strong horizontal cross-front shear was observed. As a result, the eastward departure of front aloft reduced the strain along the remnant low-level front, thus allowing the waves forced by the blocking to develop. The wavelength of the frontal waves in California’s coastal zone ( $\sim 125 \text{ km}$ ) was nearly an order of magnitude smaller than that described in the previously cited observational studies, thus suggesting that blocking generated barotropic waves on a scale equivalent to the bend in the coastline. This hypothesis does not exclude that other dynamical mechanisms may have contributed to the wave development.

## 6. Conclusions

Through the integrated analysis of experimental and operational data taken across California and the eastern Pacific during CALJET on 3 February 1998, this study has documented the complex interactions that occurred between a shallow blocked airstream along the steep coastal orography of southern California and an intense landfalling winter storm that pummeled the coastal zone with flooding rains, strong winds, and major beach erosion. A summary of these interactions and their significance are outlined below and depicted in the conceptual schematics in Fig. 28.

The large-scale evolution of the event was characterized by the landfall of two cold fronts across California, while the primary cyclone circulation remained offshore. Most of the damaging weather in the coastal zone occurred during the passage of these fronts. The leading or primary front separated a warm-sector air mass of subtropical origin from cooler postfrontal flow, whereas the trailing or secondary front marked the leading edge of a deep-tropospheric cold-core polar air mass.

The ambient southerly flow within the cyclone warm sector was deflected westward by the steep terrain along the north coast of the Bight, resulting in a corridor of terrain-parallel flow within 75 km of the coast (Fig. 28a). This blocked airstream rounded the corner of Point Conception and then continued northwestward along the coast. The near-surface high- $\theta_e$  content in the blocked flow was comparable to the cyclone warm sector ( $\sim 318\text{--}320 \text{ K}$ ), though it was much cooler in the blocked flow than in the warm sector ( $\theta \sim 287.5 \text{ vs } 291 \text{ K}$ ). The blocked flow, which extended vertically to about 1 km MSL (i.e., near the top of the local terrain), contained a  $6\text{--}8 \text{ m s}^{-1}$  barrier-jet perturbation at about 500 m MSL. It was capped by enhanced thermodynamic stratification and vertical wind shear (Fig. 28b).

Blocking modified the landfalling cold fronts and their attendant LLJs and precipitation systems in the coastal zone of southern California. Three types of modification occurred: frontal splitting, frontal merging, and

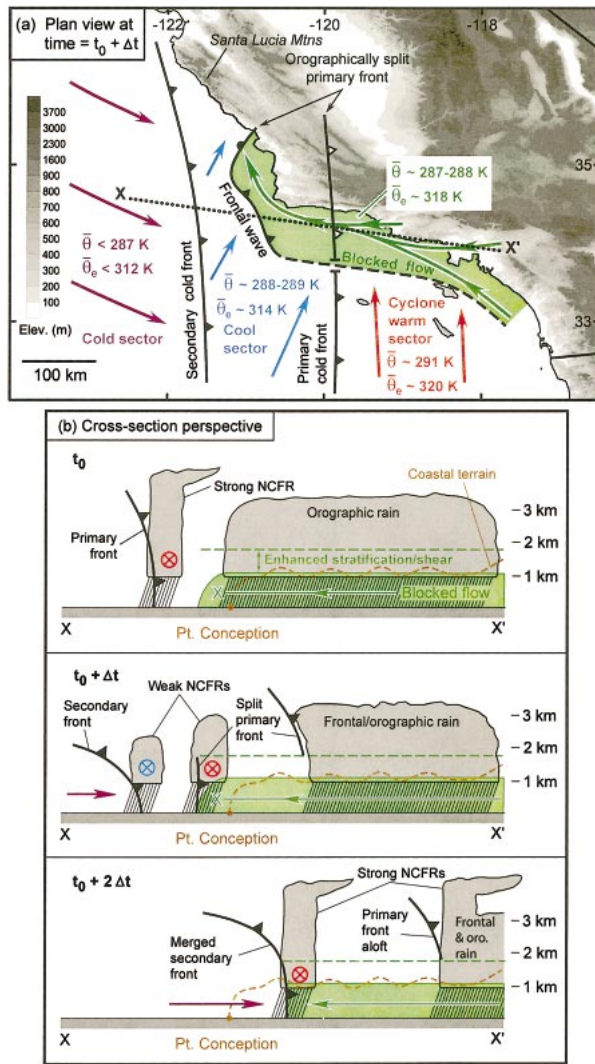


FIG. 28. (a) Plan view conceptual representation of shallow blocked flow modifying the landfalling primary cold front at  $t_0 + \Delta t$  on 3 Feb 1998. Airstreams are color-coded, and representative near-surface values of  $\theta$  and  $\theta_e$  for each air mass are shown. Dotted line  $XX'$  is a cross-section projection for (b). Terrain is shaded (see key). (b) Schematic cross sections [along  $XX'$  in (a)] highlighting the modification of the primary and secondary cold fronts and their attendant precipitation features by the blocked flow at times  $t_0$ ,  $t_0 + \Delta t$ , and  $t_0 + 2\Delta t$  (where  $\Delta t \approx 3$  h). Open and circumscribed  $\times$  symbols denote blocked flow into the page and low-level jets into the page, respectively. Color-coded airstreams are as in (a). The brown dashed line portrays the mountain profile along the north coast of the California Bight.

frontal waves. The primary cold front split in the vertical as it advanced eastward beyond the western edge of the shallow blocked air mass (Fig. 28b, at times  $t_0$  and  $t_0 + \Delta t$ ), because the airstream behind the front ( $\theta \sim 288.5$  K; Fig. 28a) was unable to mix downward through the cooler ( $\theta \sim 287.5$  K) blocked airstream. (A similar episode of frontal splitting occurred when the secondary front encountered cold blocked flow in the Los Angeles Basin after time  $= t_0 + 2\Delta t$  in Fig. 28b.) As a result,

the decoupled lower-tropospheric segment of the front (i.e., the remnant low-level primary front) remained fixed at the western periphery of the blocked airstream while, aloft, the front tracked eastward with its deep frontal precipitation system atop the stably stratified blocked flow. Farther west, the moisture-laden prefrontal LLJ remained dynamically linked to the remnant front at the western edge of the blocked flow rather than migrating eastward with the parent front aloft. A well-defined NCFR coincided with the position of the remnant front, which possessed a shallow frontal circulation.

The remnant front evolved into a pair of terrain-forced frontal waves ( $\sim 125$ -km wavelength) along the western periphery of the blocked flow over California's coastal waters (Fig. 28a depicts one such wave). These waves possessed classical thermodynamic and kinematic signatures typical of larger-scale frontal waves, including a high- $\theta_e$  warm sector flanked by a warm front with widespread precipitation and a cold front with broken-line convection. The asymmetric distribution of precipitation was attributable to the reorientation of the front by the waves. The frontal waves not only had a profound impact on the redistribution of precipitation offshore but also in the coastal mountains. Specifically, the waves enhanced the already heavy rains at the southern end of the Santa Lucia Mountains, resulting in extreme flooding there. These waves may represent a form of barotropic development arising from the removal of the frontogenic strain field when the primary cold front was split in the vertical by the shallow blocked flow, though numerical or idealized research is required to support or refute our claim.

Because the western part of the blocked air mass was warmer than that behind the secondary cold front, the secondary front was able to displace the blocked flow to the east of the nearly stationary remnant low-level primary front. Hence, blocking led to the merging of the secondary cold front with the remnant front that, in turn, profoundly impacted the secondary cold-frontal dynamics and precipitation. The secondary front evolved from a shallow-sloping boundary offshore to a nearly upright feature following its merger with the remnant front (Fig. 28b, at times  $t_0 + \Delta t$  and  $t_0 + 2\Delta t$ ). The merger significantly enhanced the low-level frontal convergence, because the blocked prefrontal airstream east of the remnant front contained a significant easterly component, whereas the unblocked prefrontal airstream offshore did not. The enhanced convergence then acted upon this blocked prefrontal flow that possessed higher values of  $\theta_e$  and greater potential instability than was observed in the unblocked prefrontal airstream prior to merging. Hence, the frontal merger resulted in an overlapping set of conditions that favored the development of a squall line that produced the largest rain rate observed anywhere in southern California during this event. Because this convective rain fell within already

saturated watersheds, flash flooding ensued in many coastal communities.

This study has important generalized implications for understanding the complex interactions that occur between shallow blocked flows and landfalling winter storms along the mountainous west coast of North America and for understanding the impact of these interactions on rainfall, winds, and erosion in the coastal zone. We hope that the knowledge gained from this study will directly benefit local forecasters along the West Coast, as well as improve numerical model forecasts in this challenging region. Operational numerical models are presently limited in their ability to resolve the structural and dynamical details of terrain-modulated flows and their interactions with fronts because of the relatively coarse spatial resolution of these models and the uncertainties associated with initializing them, especially over the ocean. These limitations result in simulations that do not adequately reflect the complexities of the real atmosphere. Through this comprehensive observational study, dynamical and physical understanding of these complicated structures, evolutions, and interactions can be advanced, and model deficiencies can be overcome, resulting in improved forecasts within orographically complex coastal zones. These results also demonstrate the importance of strategically deploying observing systems (e.g., wind profilers) in complex terrain, since blocking precludes the ability to detect frontal boundaries with only surface observations.

*Acknowledgments.* CALJET was made possible by the dedicated participation of many individuals from numerous organizations. Special thanks are given to Clark King and the rest of NOAA/ETL's field team for deploying and maintaining the wind profiler network and to Dan Gottas for processing the profiler data. The P-3 flights were made possible by NOAA's Aircraft Operations Center and the flight teams. David White of NOAA/ETL assisted in the processing of P-3 airborne radar data. Rob Hartman of the California–Nevada River Forecast Center provided the ALERT rain gauge data. Jim Adams provided quality drafting services. The collection of data and this study were supported by NOAA Research, NOAA/ETL, the U.S. Weather Research Program, and NASA's EOS Interdisciplinary Science Program. The insightful comments by Jian-Wen Bao and Bob Banta of NOAA/ETL and by two anonymous reviewers improved the scope and quality of this manuscript.

#### REFERENCES

- Andrews, E. D., R. C. Antweiler, P. J. Neiman, and F. M. Ralph, 2004: Influence of ENSO on flood frequency along the California coast. *J. Climate*, **17**, 337–348.
- Bell, G. D., and L. F. Bosart, 1988: Appalachian cold-air damming. *Mon. Wea. Rev.*, **116**, 137–161.
- Bergeron, T., 1937: On the physics of fronts. *Bull. Amer. Meteor. Soc.*, **18**, 265–275.
- Biggerstaff, M. I., and R. A. Houze, 1993: Kinematics and microphysics of the transition zone of the 10–11 June 1985 squall line. *J. Atmos. Sci.*, **50**, 3091–3110.
- Bishop, C. H., and A. J. Thorpe, 1994a: Frontal wave stability during moist deformation frontogenesis. Part I: Linear wave dynamics. *J. Atmos. Sci.*, **51**, 852–873.
- , and —, 1994b: Frontal wave stability during moist deformation frontogenesis. Part II: The suppression of nonlinear wave development. *J. Atmos. Sci.*, **51**, 874–888.
- Bjerknes, J., and H. Solberg, 1921: Meteorological conditions for the formation of rain. *Geofys. Publ.*, **2**, 1–60.
- Bond, N. A., and Coauthors, 1997: The coastal observation and simulation with topography (COAST) experiment. *Bull. Amer. Meteor. Soc.*, **78**, 1941–1955.
- Braun, S. A., R. A. Houze Jr., and B. F. Smull, 1997: Airborne dual-Doppler observations of an intense frontal system approaching the Pacific Northwest coast. *Mon. Wea. Rev.*, **125**, 3131–3156.
- , R. Rotunno, and J. B. Klemp, 1999a: Effects of coastal orography on landfalling cold fronts. Part I: Dry, inviscid dynamics. *J. Atmos. Sci.*, **56**, 517–533.
- , —, and —, 1999b: Effects of coastal orography on landfalling cold fronts. Part II: Effects of surface friction. *J. Atmos. Sci.*, **56**, 3366–3384.
- Browning, K. A., and R. Wexler, 1968: The determination of kinematic properties of a wind field using Doppler radar. *J. Appl. Meteor.*, **7**, 105–113.
- , and T. W. Harrold, 1970: Air motion and precipitation growth at a cold front. *Quart. J. Roy. Meteor. Soc.*, **96**, 369–389.
- Carter, D. A., K. S. Gage, W. L. Ecklund, W. M. Angevine, P. E. Johnston, A. C. Riddle, J. S. Wilson, and C. R. Williams, 1995: Developments in UHF lower tropospheric wind profiling at NOAA's Aeronomy Laboratory. *Radio Sci.*, **30**, 997–1001.
- Chaboureaud, J.-P., and A. J. Thorpe, 1999: Frontogenesis and the development of secondary wave cyclones during FASTEX. *Quart. J. Roy. Meteor. Soc.*, **125**, 925–940.
- Charba, J., 1974: Application of a gravity current model to analysis of squall-line gust front. *Mon. Wea. Rev.*, **102**, 140–156.
- Chien, F.-C., C. F. Mass, and P. J. Neiman, 2001: An observational and numerical study of an intense landfalling cold front along the northwest coast of the United States during COAST IOP2. *Mon. Wea. Rev.*, **129**, 934–955.
- Colle, B. A., and C. F. Mass, 1995: The structure and evolution of cold surges east of the Rocky Mountains. *Mon. Wea. Rev.*, **123**, 2577–2610.
- , B. F. Smull, and M.-J. Yang, 2002: Numerical simulations of a landfalling cold front observed during COAST: Rapid evolution and responsible mechanisms. *Mon. Wea. Rev.*, **130**, 1945–1966.
- Crum, T. D., R. L. Alberty, and D. W. Burgess, 1993: Recording, archiving, and using WSR-88D data. *Bull. Amer. Meteor. Soc.*, **74**, 645–653.
- Doyle, J. D., 1997: The influence of mesoscale coastal orography on a coastal jet and rainband. *Mon. Wea. Rev.*, **125**, 1465–1488.
- , and N. A. Bond, 2001: Research aircraft observations and numerical simulations of a warm front approaching Vancouver Island. *Mon. Wea. Rev.*, **129**, 978–998.
- Dritschel, D. G., P. H. Haynes, M. N. Jukes, and T. G. Shepherd, 1991: The stability of a two-dimensional vorticity filament under uniform strain. *J. Fluid Mech.*, **230**, 647–665.
- Dunn, L., 1987: Cold air damming by the Front Range of the Colorado Rockies and its relationship to locally heavy snows. *Wea. Forecasting*, **2**, 177–189.
- Durran, D. R., 1986: Mountain waves. *Mesoscale Meteorology and Forecasting*, P. S. Ray, Ed., Amer. Meteor. Soc., 472–492.
- Ecklund, W. L., D. A. Carter, and B. B. Balsley, 1988: A UHF wind profiler for the boundary layer: Brief description and initial results. *J. Atmos. Oceanic Technol.*, **5**, 432–441.

- Egger, J., and K. P. Hoinka, 1992: Fronts and orography. *Meteor. Atmos. Phys.*, **48**, 3–36.
- Goff, R. C., 1976: Vertical structure of thunderstorm outflows. *Mon. Wea. Rev.*, **104**, 1429–1440.
- Hobbs, P. V., and K. R. Biswas, 1979: The cellular structure of narrow cold-frontal rainbands. *Quart. J. Roy. Meteor. Soc.*, **105**, 723–727.
- , and P. O. G. Persson, 1982: The mesoscale and microscale structure and organization of clouds and precipitation in mid-latitude cyclones. Part V: The substructure of narrow cold-frontal rainbands. *J. Atmos. Sci.*, **39**, 280–295.
- Houze, R. A., and S. Medina, 2002: Comparison of orographic precipitation in MAP and IMPROVE II. Preprints, *10th Conf. on Mountain Meteorology*, Park City, UT, Amer. Meteor. Soc., 145–148. [Available from University of Washington, Department of Atmospheric Sciences, Box 351640, Seattle, WA 98195-1640.]
- James, P. K., and K. A. Browning, 1979: Mesoscale structure of line convection at surface cold fronts. *Quart. J. Roy. Meteor. Soc.*, **105**, 371–382.
- Jorgensen, D. P., T. Matejka, and J. D. DuGranrut, 1996: Multi-beam techniques for deriving wind fields from airborne Doppler radars. *J. Meteor. Atmos. Phys.*, **59**, 83–104.
- , Z. Pu, P. O. G. Persson, and W.-K. Tao, 2003: Variations associated with cores and gaps of a Pacific narrow cold frontal rainband. *Mon. Wea. Rev.*, **131**, 2705–2729.
- Klazura, G. E., and D. A. Imy, 1993: A description of the initial set of analysis products available from the NEXRAD WSR-88D system. *Bull. Amer. Meteor. Soc.*, **74**, 1293–1311.
- Kurz, M., 1990: The influence of the Alps on structure and behaviour of cold fronts over southern Germany. *Meteor. Atmos. Phys.*, **43**, 61–68.
- Locatelli, J. D., J. E. Martin, and P. V. Hobbs, 1995: Development and propagation of precipitation cores on cold fronts. *Atmos. Res.*, **38**, 177–206.
- Loehrer, S. M., and R. H. Johnson, 1995: Surface pressure and precipitation life cycle characteristics of PRE-STORM mesoscale convective systems. *Mon. Wea. Rev.*, **123**, 600–621.
- Marwitz, J. D., 1983: The kinematics of orographic airflow during Sierra storms. *J. Atmos. Sci.*, **40**, 1218–1227.
- Matejka, T. J., R. A. Houze, and P. V. Hobbs, 1980: Microphysics and dynamics of clouds associated with mesoscale rainbands in extratropical cyclones. *Quart. J. Roy. Meteor. Soc.*, **106**, 29–56.
- Mendell, T., 1992: Integration of automated hydrological data. Preprints, *Conf. on Interdisciplinary Approaches in Hydrology and Hydrogeology*, Portland, OR, American Society of Civil Engineers. [Available from NOAA/California–Nevada River Forecast Center, 3310 El Camino Ave., Sacramento, CA 95821-6308.]
- Michelson, S. A., and J.-W. Bao, 2001: Sensitivity of numerical simulations of mesoscale features associated with a land-falling cyclone to model physics. NOAA Tech. Memo. OAR ETL-302, Environmental Technology Laboratory, Boulder, CO, 38 pp. [Available from the National Technical Information Service, 5285 Point Royal Rd., Springfield, VA 22161.]
- NCDC, 1998: *Storm Data*. Vol. 40, No. 2. National Climatic Data Center, 188 pp.
- Neiman, P. J., and R. M. Wakimoto, 1999: The interaction of a Pacific cold front with shallow air masses east of the Rocky Mountains. *Mon. Wea. Rev.*, **127**, 2102–2127.
- , F. M. Ralph, M. A. Shapiro, B. F. Smull, and D. Johnson, 1998: An observational study of fronts and frontal mergers over the continental United States. *Mon. Wea. Rev.*, **126**, 2521–2554.
- , —, A. B. White, D. A. Kingsmill, and P.O.G. Persson, 2002: The statistical relationship between upslope flow and rainfall in California's coastal mountains: Observations during CALJET. *Mon. Wea. Rev.*, **130**, 1468–1492.
- Neiman, S. J., W. P. Menzel, C. M. Hayden, D. Gray, S. T. Wanzong, C. S. Velden, and J. Daniels, 1997: Fully automated cloud-drift winds in NESDIS operations. *Bull. Amer. Meteor. Soc.*, **78**, 1121–1133.
- Nuss, W. A., and D. K. Miller, 2001: Mesoscale predictability under various synoptic regimes. *Nonlinear Process. Geophys.*, **25**, 429–438.
- O'Handley, C., and L. F. Bosart, 1996: The impact of the Appalachian Mountains on cyclonic weather systems. Part I: A climatology. *Mon. Wea. Rev.*, **124**, 1353–1373.
- Overland, J. E., and N. A. Bond, 1995: Observations and scale analysis of coastal wind jets. *Mon. Wea. Rev.*, **123**, 2934–2941.
- Pandey, G. R., D. R. Cayan, and K. P. Georgakakos, 1999: Precipitation structure in the Sierra Nevada of California during winter. *J. Geophys. Res.*, **104**, 12 019–12 030.
- Panofsky, H. A., and J. A. Dutton, 1984: *Atmospheric Turbulence—Models and Methods for Engineering Applications*. Wiley-Interscience, 297 pp.
- Parish, T. R., 1982: Barrier winds along the Sierra Nevada mountains. *J. Appl. Meteor.*, **21**, 925–930.
- Parsons, D. B., and P. V. Hobbs, 1983: The mesoscale and microscale structure and organization of clouds and precipitation in mid-latitude cyclones. Part VII: Formation, development, interaction, and dissipation of rainbands. *J. Atmos. Sci.*, **40**, 559–579.
- Persson, P. O. G., F. M. Ralph, P. J. Neiman, C. King, A. B. White, and B. Walter, 1999: Observations of the structure of the low-level jet in landfalling winter storms using the CALJET observational network. Preprints, *Third Symp. on Integrated Observing Systems*, Dallas, TX, Amer. Meteor. Soc., 82–85. [Available from NOAA/Environmental Technology Laboratory, Mail Code R/ET7, 325 Broadway, Boulder, CO 80305.]
- Peterson, T. C., L. O. Grant, W. R. Cotton, and D. C. Rogers, 1991: The effect of decoupled low-level flow on winter orographic clouds and precipitation in the Yampa River valley. *J. Appl. Meteor.*, **30**, 368–386.
- Pierrehumbert, R. T., and B. Wyman, 1985: Upstream effects of mesoscale mountains. *J. Atmos. Sci.*, **42**, 977–1003.
- Rabin, R., and D. Zrnica, 1980: Subsynoptic-scale vertical wind revealed by dual Doppler radar and VAD analysis. *J. Atmos. Sci.*, **37**, 644–654.
- Ralph, F. M., P. J. Neiman, D. W. van de Kamp, and D. C. Law, 1995: Using spectral moment data from NOAA's 404-MHz radar wind profilers to observe precipitation. *Bull. Amer. Meteor. Soc.*, **76**, 1717–1739.
- , and Coauthors, 1999: The California Land-falling Jets Experiment (CALJET): Objectives and design of a coastal atmosphere–ocean observing system deployed during a strong El Niño. Preprints, *Third Symp. on Integrated Observing Systems*, Dallas, TX, Amer. Meteor. Soc., 78–81. [Available from NOAA/ETL, Mail Code R/ET7, 325 Broadway, Boulder, CO 80305.]
- , and Coauthors, 2003: The impact of a prominent rain shadow on flooding in California's Santa Cruz Mountains: A CALJET case study and sensitivity to the ENSO cycle. *J. Hydrometeorol.*, **4**, 1243–1264.
- Renfrew, I. A., A. J. Thorpe, and C. H. Bishop, 1997: The role of the environmental flow in the development of secondary frontal cyclones. *Quart. J. Roy. Meteor. Soc.*, **123**, 1653–1675.
- Reynolds, D. W., and A. P. Kuciauskas, 1988: Remote and in situ observations of Sierra Nevada winter mountain clouds: Relationships between mesoscale structure, precipitation and liquid water. *J. Appl. Meteor.*, **27**, 140–156.
- Rotunno, R., J. B. Klemp, and M. L. Weisman, 1988: A theory for strong, long-lived squall lines. *J. Atmos. Sci.*, **45**, 463–485.
- Schumacher, P. N., D. J. Knight, and L. F. Bosart, 1996: Frontal interaction with the Appalachian Mountains. Part I: A climatology. *Mon. Wea. Rev.*, **124**, 2453–2468.
- Schwartz, B. E., S. G. Benjamin, S. M. Green, and M. R. Jardin, 2000: Accuracy of RUC-1 and RUC-2 wind and aircraft trajectory forecasts by comparison with ACARS observations. *Wea. Forecasting*, **15**, 313–326.
- Sinclair, M. R., D. S. Wratt, R. D. Henderson, and W. R. Gray, 1997: Factors affecting the distribution and spillover of precipitation in the Southern Alps of New Zealand—A case study. *J. Appl. Meteor.*, **36**, 428–442.

- Smith, R. B., 1979: The influence of mountains on the atmosphere. *Advances in Geophysics*, Vol. 21, Academic Press, 87–230.
- Smolarkiewicz, P. K., and R. Rotunno, 1990: Low Froude number flow past three-dimensional obstacles. Part II: Upwind flow reversal zone. *J. Atmos. Sci.*, **47**, 1498–1511.
- Smull, B. F., and R. A. Houze, 1987: Rear inflow in squall lines with trailing stratiform precipitation. *Mon. Wea. Rev.*, **115**, 2869–2889.
- Stumpf, G. J., R. H. Johnson, and B. F. Smull, 1991: The wake low in a midlatitude convective system having complex convective organization. *Mon. Wea. Rev.*, **119**, 134–158.
- Velden, C. S., C. M. Hayden, S. J. Neiman, W. P. Menzel, S. Wanzong, and J. S. Goerss, 1997: Upper-tropospheric winds derived from geostationary satellite water vapor observations. *Bull. Amer. Meteor. Soc.*, **78**, 173–195.
- Wakimoto, R. M., and B. L. Bosart, 2000: Airborne radar observations of a cold front during FASTEX. *Mon. Wea. Rev.*, **128**, 2447–2470.
- Weber, B. L., D. B. Wuertz, D. C. Welsh, and R. McPeck, 1993: Quality controls for profiler measurements of winds and RASS temperatures. *J. Atmos. Oceanic Technol.*, **10**, 452–464.
- Wentz, F. J., 1997: A well-calibrated ocean algorithm for special sensor microwave/imager. *J. Geophys. Res.*, **102**, 8703–8718.
- White, A. B., D. J. Gottas, E. Strem, F. M. Ralph, and P. J. Neiman, 2002: An automated brightband height detection algorithm for use with Doppler radar spectral moments. *J. Atmos. Oceanic Technol.*, **19**, 687–697.
- , P. J. Neiman, F. M. Ralph, D. E. Kingsmill, and P. O. G. Persson, 2003: Coastal orographic rainfall processes observed by radar during the California Land-falling Jets Experiment. *J. Hydro-meteor.*, **4**, 264–282.
- Yu, C.-K., and B. F. Smull, 2000: Airborne Doppler observations of a landfalling cold front upstream of steep coastal orography. *Mon. Wea. Rev.*, **128**, 1577–1603.
- , and N. A. Bond, 2002: Airborne Doppler observations of a cold front in the vicinity of Vancouver Island. *Mon. Wea. Rev.*, **130**, 2692–2708.